H0LiCOW – V. New COSMOGRAIL time delays of HE 0435−1223: H_0 to 3.8 per cent precision from strong lensing in a flat ΛCDM model

V. Bonvin,[1]★ F. Courbin,[1] S. H. Suyu,[2,3,4] P. J. Marshall,[5] C. E. Rusu,[6] D. Sluse,[7]
M. Tewes,[8] K. C. Wong,[9,4] T. Collett,[10] C. D. Fassnacht,[7] T. Treu,[11]
M. W. Auger,[12] S. Hilbert,[13,14] L. V. E. Koopmans,[15] G. Meylan,[1]
N. Rumbaugh,[11] A. Sonnenfeld[16,11,17] and C. Spiniello[2]

Affiliations are listed at the end of the paper

ABSTRACT

We present a new measurement of the Hubble Constant H_0 and other cosmological parameters based on the joint analysis of three multiply imaged quasar systems with measured gravitational time delays. First, we measure the time delay of HE 0435−1223 from 13-yr light curves obtained as part of the COSMOGRAIL project. Companion papers detail the modelling of the main deflectors and line-of-sight effects, and how these data are combined to determine the time-delay distance of HE 0435−1223. Crucially, the measurements are carried out blindly with respect to cosmological parameters in order to avoid confirmation bias. We then combine the time-delay distance of HE 0435−1223 with previous measurements from systems B1608+656 and RXJ1131−1231 to create a Time Delay Strong Lensing probe (TDSL). In flat Λ cold dark matter (ΛCDM) with free matter and energy density, we find $H_0 = 71.9^{+2.4}_{-3.0}$ km s^{-1} Mpc^{-1} and $\Omega_\Lambda = 0.62^{+0.24}_{-0.35}$. This measurement is completely independent of, and in agreement with, the local distance ladder measurements of H_0. We explore more general cosmological models combining TDSL with other probes, illustrating its power to break degeneracies inherent to other methods. The joint constraints from TDSL and Planck are $H_0 = 69.2^{+1.4}_{-2.2}$ km s^{-1} Mpc^{-1}, $\Omega_\Lambda = 0.70^{+0.01}_{-0.01}$ and $\Omega_k = 0.003^{+0.004}_{-0.006}$ in open ΛCDM and $H_0 = 79.0^{+4.4}_{-4.2}$ km s^{-1} Mpc^{-1}, $\Omega_{de} = 0.77^{+0.02}_{-0.03}$ and $w = -1.38^{+0.14}_{-0.16}$ in flat wCDM. In combination with Planck and baryon acoustic oscillation data, when relaxing the constraints on the numbers of relativistic species we find $N_{eff} = 3.34^{+0.21}_{-0.21}$ in $N_{eff}\Lambda$CDM and when relaxing the total mass of neutrinos we find $\Sigma m_\nu \leq 0.182$ eV in $m_\nu\Lambda$CDM. Finally, in an open wCDM in combination with Planck and cosmic microwave background lensing, we find $H_0 = 77.9^{+5.0}_{-4.2}$ km s^{-1} Mpc^{-1}, $\Omega_{de} = 0.77^{+0.03}_{-0.03}$, $\Omega_k = -0.003^{+0.004}_{-0.004}$ and $w = -1.37^{+0.18}_{-0.23}$.

Key words: gravitational lensing: strong – galaxies: individual: HE 0435−1223 – cosmology: observations – distance scale.

1 INTRODUCTION

In the past decade, the Standard Cosmological Model, Λ cold dark matter (ΛCDM), which assumes the existence of either a cosmological constant or a form of dark energy with equation of state $w = -1$, and large-scale structure predominantly composed of cold dark matter, has been firmly established given observations to date (e.g. Hinshaw et al. 2013; Planck Collaboration XIII 2016a). From a minimal set of six parameters describing ΛCDM, one can in principle infer the value of other parameters such as the current expansion rate of the Universe, H_0. However, such an inference

involves strong assumptions about the cosmological model, such as the absence of curvature or a constant equation of state for the dark energy. Conversely, we can relax these assumptions and explore models beyond flat ΛCDM using a wider set of cosmological probes. In this case, the analysis benefits greatly from independent measurements of H_0 from observations of distance probes such as the distance ladder or water masers (see e.g. Treu 2010; Weinberg et al. 2013; Treu & Marshall 2016, for a review). As Weinberg et al. (2013) point out, the figure of merit of any stage III or stage IV cosmological survey improves by 40 per cent if an independent measurement of H_0 is available to a precision of 1 per cent.

The 'time-delay distances' in gravitationally lensed quasar systems offer an opportunity to measure H_0 independently of any

other cosmological probe. First suggested by Refsdal (1964), this approach involves measuring the time delays between multiple images of a distant source produced by a foreground lensing object. The time delays depend on the matter distribution in the lens (galaxy), on the overall matter distribution along the line of sight and on the cosmological parameters. The time delays are related to the so-called time-delay distance $D_{\Delta t}$ to the lens and the source, which is primarily sensitive to H_0 and has a weak dependence on the matter density Ω_m, the dark energy density Ω_{de}, the dark energy equation of state, w, and on the curvature parameter Ω_k (e.g. Suyu et al. 2010; Linder 2011).

The first critical step for the method to work is the measurement of the time delays from a photometric monitoring campaign to measure the shift in time between the light curves of the lensed images of quasars. Such monitoring campaigns must be long enough, and have good enough temporal sampling, to catch all possible (and usually small) photometric variations in the light curves. This is the goal of the COSMOGRAIL collaboration: the COSmological MOnitoring of GRAvItational Lenses, which has been monitoring about 20 lensed quasars with 1-m class and 2-m class telescopes since 2004 (e.g. Courbin et al. 2005; Eigenbrod et al. 2006a; Bonvin et al. 2016). The target precision for the time-delay measurements is a few per cent or better, because the error on the time delays propagates linearly to the first order on the cosmological distance measurement. Examples of COSMOGRAIL results include Courbin et al. (2011), Tewes et al. (2013b), Rathna Kumar et al. (2013) and Eulaers et al. (2013).

The second critical step is the modelling of the lens galaxy. Indeed, time-delay measurements alone can constrain only a combination of the time-delay distance and the surface density of the lens around the quasar images (Kochanek 2002). Additional constraints on the density profile of the lens are therefore required in order to convert observed time delays into inferences of the time-delay distance. These constraints can be derived from velocity dispersion measurements, and the radial magnification of the extended, lensed arc image of the quasar host galaxy (e.g. Suyu et al. 2010, 2014). Ideal targets for this purpose are lensed quasars with a prominent host, which offer strong constraints on the density profile slope of the foreground lens.

In modelling the lens mass distribution, special care has to be paid to the mass-sheet degeneracy (MSD), and, more generally, the source-position transformation (SPT; e.g. Falco, Gorenstein & Shapiro 1985; Wucknitz 2002; Schneider & Sluse 2013, 2014; Unruh, Schneider & Sluse 2016; Xu et al. 2016). These can be seen as degeneracies in the choice of the gravitational lensing potential that leave all the lensing observables invariant except for the modelled time delay, Δt. In other words, a wrong model of the main lens mass distribution can perfectly fit the observed morphology of the lensing system, and yet result in an inaccurate inference of the time-delay distance. Priors and spectroscopic constraints on the dynamics of the main lens therefore play a critical role in avoiding systematic biases. In addition, perturbations to the lens potential by the distribution of mass along the line of sight also creates degeneracies in the lens modelling. The latter can be mitigated with a measurement of the mass distribution along the line of sight, for example by using spectroscopic redshift measurements of the galaxies in the lens environment (e.g. Fassnacht et al. 2006; Wong et al. 2011), comparisons between galaxy number counts in the real data and in simulations (Hilbert et al. 2007, 2009; Fassnacht, Koopmans & Wong 2011; Collett et al. 2013; Greene et al. 2013; Suyu et al. 2013; McCully et al. 2016) or using weak-lensing measurements (Tihonova et al., in preparation)

The H0LiCOW collaboration (H_0 Lenses in COSMOGRAIL's Wellspring) capitalizes on the efforts of COSMOGRAIL to measure accurate time delays, and on high-quality auxiliary data from *Hubble Space Telescope* (*HST*) and 10-m class ground-based telescopes, to constrain cosmology. The H0LiCOW sample consists of five well-selected targets, each with exquisite time-delay measurements. B1608+656, monitored in radio band with the VLA (Fassnacht et al. 2002), and RXJ1131−1231, monitored by COSMOGRAIL in the visible (Tewes et al. 2013b), have already shown promising results, with relative precisions on the time-delay distance of 5 and 6.6 per cent, respectively (Suyu et al. 2010, 2014).

This paper is part of the H0LiCOW series, focusing on the quadruple lensed quasar HE 0435−1223 (α(2000): $04^h38^m14\overset{s}{.}9$; δ(2000): $-12°17'14\overset{''}{.}4$) (Wisotzki et al. 2000, 2002) discovered during the Hamburg/ESO Survey (HES) for bright quasars in the Southern hemisphere. The source redshift has been measured by Sluse et al. (2012) as $z_s = 1.693$, and the redshift of the lens has been measured by Morgan et al. (2005) and Eigenbrod et al. (2006b) as $z_d = 0.4546 \pm 0.0002$. The lens lies in a group of galaxies of at least 12 members. A first measurement of the time delay for HE 0435−1223 was presented in Courbin et al. (2011). In this work, we present a significant improvement of the time-delay measurement, with twice as long light curves as in Courbin et al. (2011). The other H0LiCOW papers include an overview of the project (Suyu et al., submitted; hereafter H0LiCOW Paper I), a spectroscopic survey of the field of HE 0435−1223 and a characterization of the groups along the line of sight (Sluse et al., submitted; hereafter H0LiCOW Paper II), a photometric survey of the field of HE 0435−1223 with an estimate of the effect of the external line-of-sight structure (Rusu et al., submitted; hereafter H0LiCOW Paper III), and a detailed modelling of the lens and the inference of the time-delay distance along with cosmological results for HE 0435−1223 (Wong et al., in press; hereafter H0LiCOW Paper IV). In this paper, we combine the results for HE 0435−1223 with those from the other two lensed quasars already published, and with other cosmological data sets (Bennett et al. 2013; Hinshaw et al. 2013; Planck Collaboration XIII 2016a).

This paper is organized as follows. Section 2 presents the COSMOGRAIL optical monitoring data and its reduction process. Section 3 presents the time-delay measurements and related uncertainties. Section 4 summarizes the main steps of the field-of-view analysis detailed in H0LiCOW Paper II and H0LiCOW Paper III and the lens modelling detailed in H0LiCOW Paper IV that lead to the time-delay distance determination. Section 5 combines the time-delay distance of HE 0435−1223 and other lenses, and with additional cosmological data sets, in order to make the best possible inferences of cosmological parameters. Finally, Section 6 presents our conclusions and future prospects in the light of these results.

2 PHOTOMETRIC MONITORING DATA

HE 0435−1223 has been monitored since 2003 as part of the COSMOGRAIL programme and in collaboration with the Kochanek et al. (2006) team. The data acquired from autumn 2003 to spring 2010 were presented in Courbin et al. (2011). Here, we double the monitoring period, adding observations taken between autumn 2010 and spring 2016. Our monitoring sites include two Northern telescopes: the 1.2 m Belgian Mercator telescope located at the Roque de Los Muchachos Observatory, La Palma, Canary Islands (Spain) and the 1.5 m telescope located at the Maidanak Observatory (Uzbekistan). The average observing cadence was 11 and 16 d, respectively, at these sites. These telescopes ceased taking data for

Table 1. Optical monitoring campaigns of HE 0435−1223. The sampling is the mean number of days between the observations, not considering the seasonal gaps.

Telescope	Camera	FoV	Pixel	Period of observation	#obs	Exp. time	Median FWHM	Sampling
Euler	C2	11 arcmin × 11 arcmin	0.344 arcsec	2004 Jan–2010 Mar	301	5 × 360 s	1.37 arcsec	6 d
Euler	ECAM	14.2 arcmin × 14.2 arcmin	0.215 arcsec	2010 Sep–2016 Mar	301	5 × 360 s	1.39 arcsec	4 d
Mercator	MEROPE	6.5 arcmin × 6.5 arcmin	0.190 arcsec	2004 Sep–2008 Dec	104	5 × 360 s	1.59 arcsec	11 d
Maidanak	SITE	8.9 arcmin × 3.5 arcmin	0.266 arcsec	2004 Oct–2006 Jul	26	10 × 180 s	1.31 arcsec	16 d
Maidanak	SI	18.1 arcmin × 18.1 arcmin	0.266 arcsec	2006 Aug–2007 Jan	8	6 × 300 s	1.31 arcsec	16 d
SMARTS	ANDICAM	10 arcmin × 10 arcmin	0.300 arcsec	2003 Aug–2005 Apr	136	3 × 300 s	≤1.80 arcsec	4 d
TOTAL	–	–	–	2003 Aug–2016 Mar	876	394.5 h	–	3.6 d

COSMOGRAIL in 2008 December. In the Southern hemisphere, the Swiss 1.2 m Euler telescope located at the ESO La Silla observatory (Chile) has monitored HE 0435−1223 since 2004. Two cameras were used: the C2 and the EulerCAM instruments, with an average cadence of 6 and 4 d, respectively. We also make use of the data obtained at the 1.3 m SMARTS ANDICAM camera at Cerro Tololo Inter-American Observatory. Note that we do not re-analyse the SMARTS data, but use directly the published photometric measurements (Kochanek et al. 2006). Table 1 gives a detailed summary of the observations.

2.1 Data reduction

The full data set consists of two distinct blocks that do not overlap in time and that we treat independently. The first block includes the Mercator, Maidanak and Euler-C2 data, to which we add the published SMARTS photometry. The detailed processing and the relative photometric calibration of these curves is presented in section 2.2 of Courbin et al. (2011). The second block consists of the 301 new data points obtained with EulerCAM that we reduce with the pipeline described in section 3 of Tewes et al. (2013b), whose main steps can be summarized as follows.

(i) Each image is corrected for bias and readout effects. We then apply a flat-field correction using a high signal-to-noise master sky-flat which we correct for a pattern generated by the shutter opening and closing times. A spatially variable sky background frame is then constructed using the SEXTRACTOR software (Bertin & Arnouts 1996) and we subtract it from the data frame. All the frames are aligned and analysed to carry out the photometric measurements. Fig. 1 presents a stack of the 100 EulerCAM images with a seeing smaller than 1.14 arcsec.

(ii) The photometric measurements of the four blended images of HE 0435−1223 are obtained using deconvolution photometry using the MCS deconvolution algorithm (Magain, Courbin & Sohy 1998; Cantale et al. 2016). To do this, the point spread function (PSF) is measured, for each exposure individually, using the seven stars labelled PSF1–PSF7 on Fig. 1. A simultaneous deconvolution of all the frames is then carried out, leading to a model composed of a deep image representing extended sources, and a catalogue of point sources with improved resolution and sampling. During the deconvolution process, the data are decomposed into a sum of analytical point sources (the quasar images) and of a numerical pixel channel containing the image of the lensing galaxy and of any potential extended object.

(iii) We compute a multiplicative median normalization coefficient for each exposure, using several deconvolved reference stars. If possible at all, we use stars whose colours is similar to that of the quasar. In the case of HE 0435−1223, we use eight reference stars, labelled N1–N8 in Fig. 1. We then apply the normalization

coefficient to the deconvolved images of the point sources. Their intensities are returned for every frame, hence leading to the light curves.

The upper panel of Fig. 2 presents the 13-yr-long COSMOGRAIL light curves of HE 0435−1223, including the data from Courbin et al. (2011) and our new data. The similarity between the four light curves is immediately noticeable. However, it can also be noted that they would not superpose perfectly when shifted in time and magnitude, due to 'extrinsic variability' which is interpreted as being caused by microlensing by stars in the lensing galaxy (see e.g. Blackburne et al. 2014; Braibant et al. 2014). These extrinsic contributions are clearly seen here on time-scales from a few weeks to several years, in the form of an evolution of the magnitude-separation between the light curves. They must be handled properly in order to measure time delays with high accuracy.

2.2 On the importance of long light curves

Given the limited photometric precision of the COSMOGRAIL images, long-term monitoring is crucial to the time-delay measurement for two main reasons. First, one needs to catch enough intrinsic photometric variations in the quasar light curves in order to identify common structures. In the present case, these can be found on average two to three times per observing season, with some seasons displaying more prominent structures than others. Inflexion points in the light curves are most precious to constrain the time delays. For example, dips and peaks with an amplitude of nearly half a magnitude can be observed in several seasons: 2004–2005, 2012–2013 and 2015–2016. Secondly, the extrinsic variability related to microlensing must be taken into account (e.g. by modelling and removing it) to avoid time-delay measurement biases. Any simple and well-constrainable model is likely not sufficient to capture all aspects of this extrinsic variability, and might result in residual biases. The availability of decade long light curves allows us to check for potentially significant biases by analysing subsets of the full data, and certainly to reduce residual ones.

3 TIME-DELAY MEASUREMENT

With the light curves in hand, the time delays can be measured using numerical techniques accounting for noisy photometry, irregular temporal sampling and seasonal monitoring gaps. These techniques must also account for the extrinsic variability in the quasar images, related to microlensing effects, to avoid systematic error on the time-delay measurements. Different techniques have been devised in the literature to carry out this task, and the COSMOGRAIL collaboration has implemented its own approach and several algorithms (see Tewes, Courbin & Meylan 2013a, also for a summary of extrinsic variability causes). These techniques are
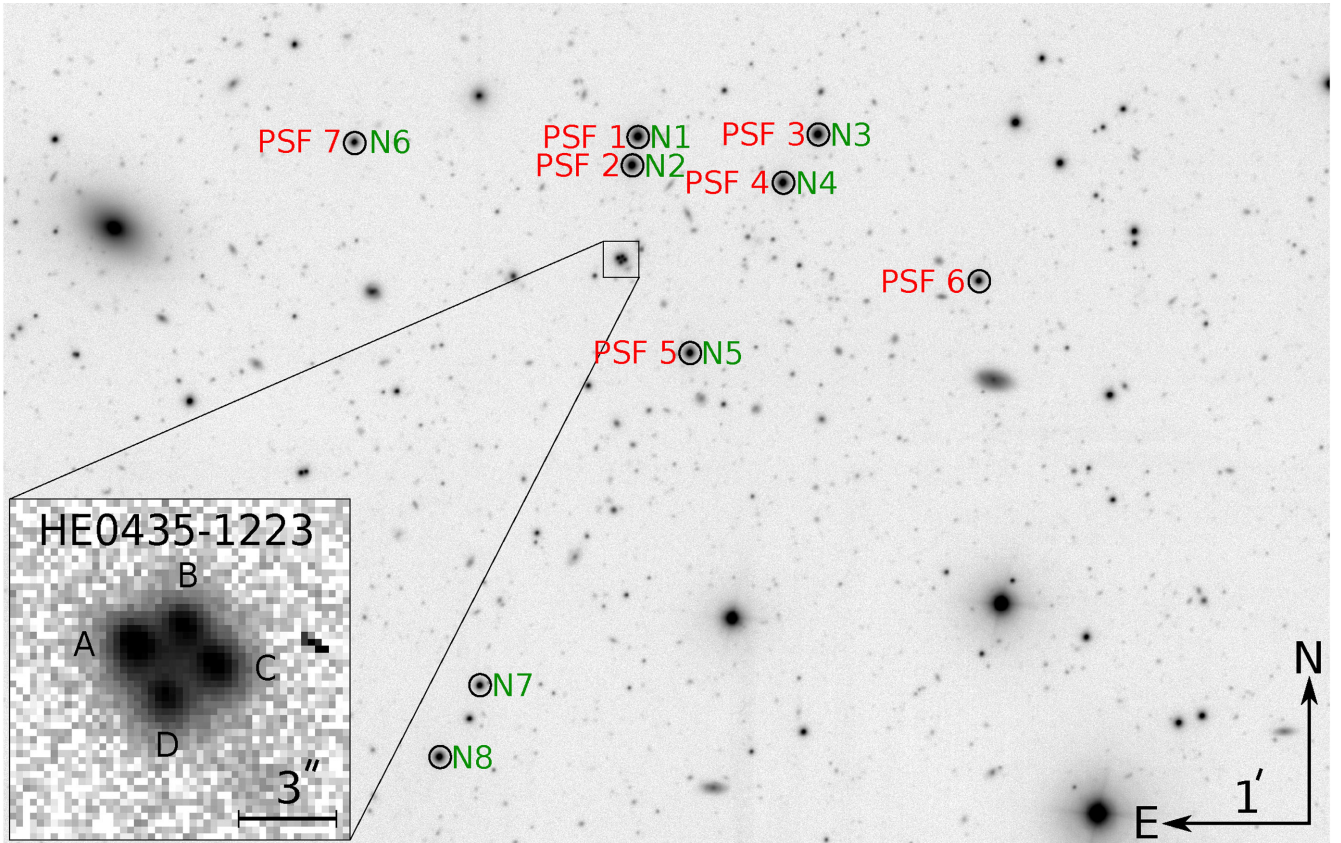
Figure 1. Part of the field of view of EulerCAM installed on the Swiss 1.2 m telescope around the quasar HE 0435−1223. This image is a combination of 100 exposures of 360 s each, for a total exposure time of 10 h. The stars used to build a PSF model for each EulerCAM exposure are circled and labelled PSF1 to PSF7 in red, and the stars used for the photometric calibrations are circled and labelled N1–N8 in green. The insert in the bottom left shows the single, 360 s exposure of the lens, for reference. Note that photometric and spectroscopic redshifts are available for many galaxies in the field of view (see H0LiCOW Paper II and H0LiCOW Paper III for details).

publicly available as a PYTHON package named PYCS.[1] They have been tested using realistic numerical simulations, and have been confronted with the data provided to the lensing community by the first Time-Delay Challenge (TDC1; see Dobler et al. 2015; Liao et al. 2015). An in-depth analysis of their performance proved them to be both precise and accurate (Bonvin et al. 2016) under various observational conditions, and in particular for light curves mimicking the COSMOGRAIL data. Among the three point-estimation algorithms provided in the PYCS toolbox, we consider for this work two algorithms based on very different principles.

(i) *The free-knot spline technique* models the light curves as a sum of intrinsic variations of the quasar, common to the four light curves, plus some extrinsic variability different in each of the four light curves. The algorithm simultaneously fits one continuous curve for the intrinsic variations, four less-flexible curves for the extrinsic variations, and time shifts between the four light curves. All curves are represented as *free-knot* splines (see e.g. Molinari, Durand & Sabatier 2004), for which the knot locations are optimized at the same time as the spline coefficients and the time shifts.

(ii) *The regression difference technique* minimizes the variability of the difference between Gaussian-process regressions performed on each light curve. This method has no explicitly parametrized

model for extrinsic variability. Instead, it yields time-delay estimates which minimize apparent extrinsic variability on time-scales comparable to that of the precious intrinsic variability features. We see the contrasting approaches of this technique and the free-knot splines as valuable to detect potential method-related biases, and will use the regression difference technique as a cross-check of our results in this paper.

The third original PYCS estimator, a dispersion technique that was inspired by Pelt et al. (1996) and used in the previous analysis of HE 0435−1223 (Courbin et al. 2011) has proven to be less accurate in several investigations of simulated data (see Eulaers et al. 2013; Rathna Kumar et al. 2013; Tewes et al. 2013a,b). For this reason, we do not consider it in this work.

We stress that the uncertainty estimation for the time delays is at least as important as the above point estimators. It is carried out within PYCS by assessing the point-estimation performance on synthetic light curves. This approach attempts to capture significantly more than the formal uncertainty which could be derived from the photometric error bars, if one would assume that for instance the spline model described above is a sufficient description of the data.

3.1 Application to the data

To apply the free-knot spline and regression difference techniques provided by PYCS to our data, we closely follow the procedure

---

[1] PYCS can be obtained from http://www.cosmograil.org
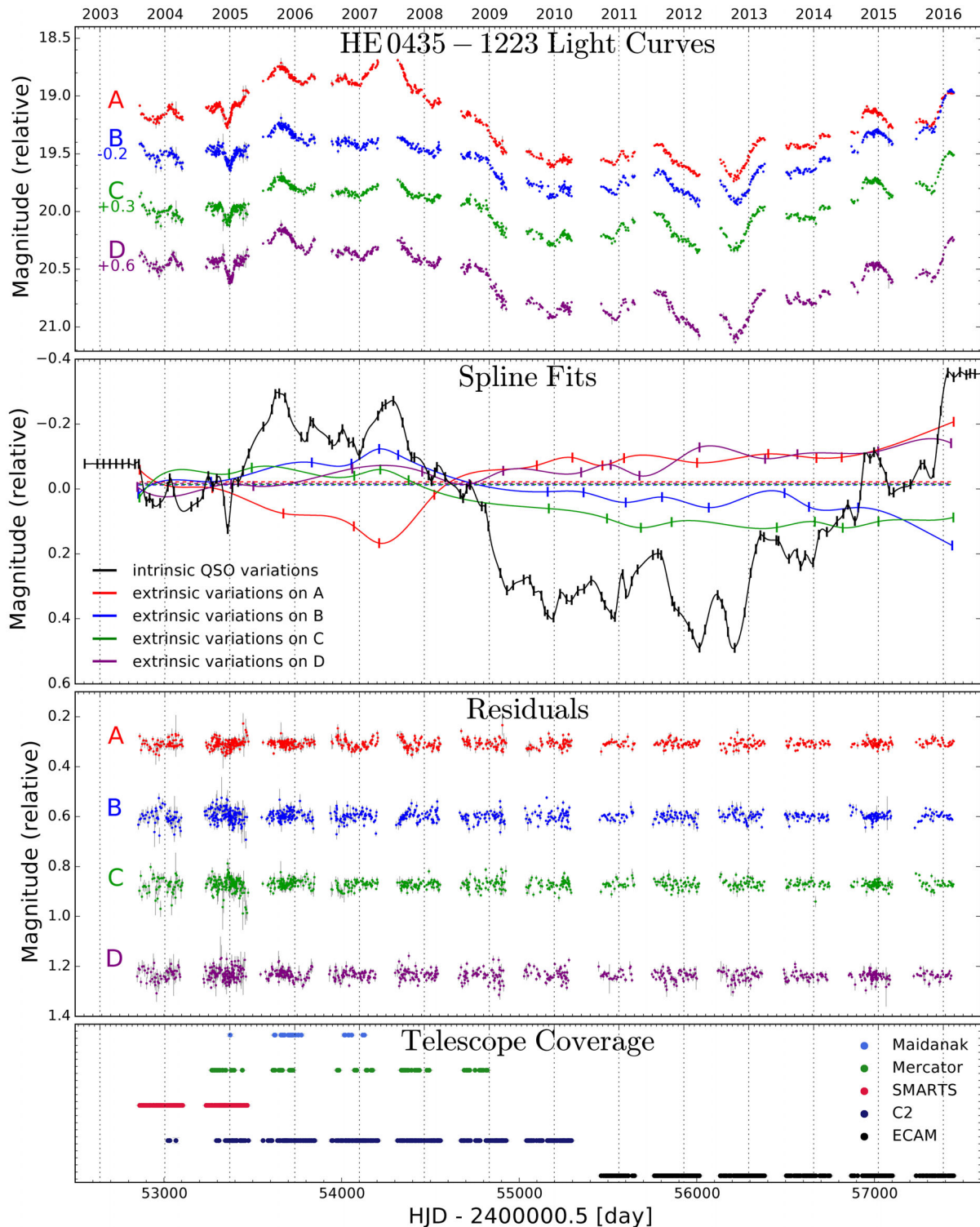
Figure 2. From top to bottom: light curves for the four lensed images of the quasar HE 0435−1223. The relative shifts in magnitude are chosen to ease visualization, and do not influence the time-delay measurements. The second panel shows a model of the intrinsic variations of the quasar (black) and the four curves for the extrinsic variations in each quasar image using the free-knot spline technique (colour code). The vertical ticks indicate the position of the spline knots. The residuals of the fits for each light curve is shown in the next panel. Finally, the bottom panel displays the journal of the observations for HE 0435−1223 for the five telescopes or cameras used to gather the data over 13 yr (see column '#obs' of Table 1), where each point represents one monitoring night. The light curves are publicly available on the H0LiCOW,[2] COSMOGRAIL[3] and CDS websites.

---

described in Tewes et al. (2013a), and summarized in the following.[4] A key ingredient of this approach is the careful generation of mock light curves which are used to fine-tune and assess the precision and bias of the point estimators. These simulations are fully synthetic, in the sense that they are drawn from models with known time delays (hereafter *true* time delays), and yet they closely mimic the quasar variability signal and the extrinsic variability from the observed data. The PYCS free-knot spline technique is used to create the generative models from which we draw these simulations. For this, we start by fitting an intrinsic spline with on average 10 knots yr^{-1} and four extrinsic splines with 2 knots yr^{-1} to the observations. These average knot densities are sufficiently high to fit all unambiguous patterns observed in the data, while still resulting in a negligible intrinsic variance, i.e. avoiding significant degeneracies between the time-delay estimates and the spline models. Such a free-knot spline fit is illustrated in the second panel of Fig. 2. The extrinsic variability splines presented here, when subtracted to each other pair-wise, are compatible with the data presented in Blackburne et al. (2014). However, we also show in our robustness checks [see point (ii) of Section 3.2] that variations in the modelling of the extrinsic variability do not influence much the time-delay measurements.

Before drawing the synthetic mock curves by sampling from this model fit, the smooth extrinsic splines are locally augmented with fast correlated noise. This noise follows a power-law spectrum which is iteratively adjusted so that the scatter in the mock curves has similar statistical properties to the scatter measured in the observed data. We then draw 1000 mock data sets, with true time shifts uniformly distributed within ±3 d around our best-fitting solution. This results in a range of ±6 d for the true delays, largely covering all plausible situations for this lens system. It is important to use simulations with various true time delays to tune and/or verify the accuracy of the point estimators. Tests on simulations with only a single true time delay would not probe bias and precision reliably, especially as many time-delay estimators are prone to responding unsteadily to the true delay.

The third panel of Fig. 2 shows the observed residual light curves after subtraction of a free-knot spline fit, and the bottom panel depicts the coverage by the different telescopes and instruments. During the first 5 yr of monitoring, three to four different telescopes were used, with a mean residual dispersion of all data points of $\sigma = 25$ mmag. During the last years (2011 to present) one telescope was used, with a mean residual dispersion of $\sigma = 15$ mmag. Besides unmodelled microlensing effects, part of this scatter comes from night-to-night and instrument-to-instrument calibration of the data. Long-term monitoring programmes of gravitational lenses are a matter of balance between the gain in temporal sampling using multiple telescopes, and the losses in photometric precision due to combining data from different instruments. Future monitoring programmes will need to account for this trade-off (Courbin et al., in preparation).

We run the free-knot spline fit and the regression difference technique (with a Matérn covariance function, an amplitude parameter of 2.0 mag, a scale of 250 d and a smoothness degree $\nu = 1.5$) on the observed light curves as well as on the mocks (for details, see Tewes et al. 2013a). Fig. 3 presents our time-delay estimates along with their 1σ uncertainties, and compares them to the previous measurements by Courbin et al. (2011), for which the dispersion technique was used. The uncertainties are computed by summing the maxi-

mum estimated bias and statistical uncertainty in quadrature. The free-knot spline technique and regression difference technique are in relatively good agreement with each other, with a maximum tension of 1.3σ. Recall that the measurements are not independent, and therefore good agreement is to be expected. The two techniques also yield a similar precision, with a 6.5 per cent relative uncertainty on the longest delay, i.e. $\Delta t_{\rm AD}$.

3.2 Robustness checks

In order to test the robustness of our time-delay measurements, we performed several simple checks.

(i) We carried out several times the deconvolution of the ECAM data, using PSF stars and/or normalization stars that differ from the ones adopted in Fig. 1. We also changed the initial parameters of the MCS deconvolution photometry. These include an estimate for the light profile of the lens galaxy, the astrometry of the quasar images and of the lens galaxy and the flux of the quasar images at each epoch. All these changes resulted in a slightly higher scatter in the ECAM light-curves data points, yet without significant impact on the time-delay measurements.

(ii) We varied the intrinsic and/or extrinsic variability model of the free-knot spline technique by changing the number of knots used. We used 8–12 knots yr^{-1} for the intrinsic model, and 0.5–2 knots yr^{-1} for the extrinsic model. Free-knot splines have the advantage over regular splines or polynomials that their ability to fit prominent variability features is less sensitive to the total number of parameters. Using a lower or higher number of knots did not significantly affect the time-delay measurements. The residual light curves (third panel of Fig. 2) remain statistically similar.

(iii) Taking advantage of the 13 yr of monitoring, we split the light curves into three parts: (i) seasons 2003–2004 to 2006–2007, (ii) seasons 2007–2008 to 2011–2012 and (iii) seasons 2012–2013 to 2015–2016. We measured the time delays independently on each of these subsections. The results are presented in the bottom parts of each panel of Fig. 3. We see that the measurements on these subsections are well distributed around the delays measured on the full light curves. Furthermore, a clear majority of the delays obtained on the subsections cover, within the given 1σ error estimates, the results from the full curves. To conclude, these robustness checks give no strong evidence that the achieved time-delay uncertainties are significantly underestimated and/or biased.

3.3 Time delays of HE 0435−1223

We have shown that our two curve shifting techniques lead to comparable time delays and error bars on the full light curves of HE 0435−1223, which is reassuring. Still, one needs to define which time-delay estimates to propagate into the time-delay distance (H0LiCOW Paper IV) and cosmological parameter inferences. We opt for using the results from the free-knot spline technique. This method has been tested extensively on a broad range of simulated light curves and proved to be both precise and accurate (Bonvin et al. 2016). In addition, Sluse & Tewes (2014) showed with this same technique that a flexible extrinsic variability model can prevent potential time-delay biases due to the delayed emission of the broad-line region of the quasar with respect to the accretion disc.

4 TIME-DELAY DISTANCE

The time delays determined in Section 3, combined with a careful modelling of the lens galaxy mass distribution, can be used to infer

---

[4] For the sake of reproducibility, the complete PYTHON code used to measure the delays is available at http://www.cosmograil.org.
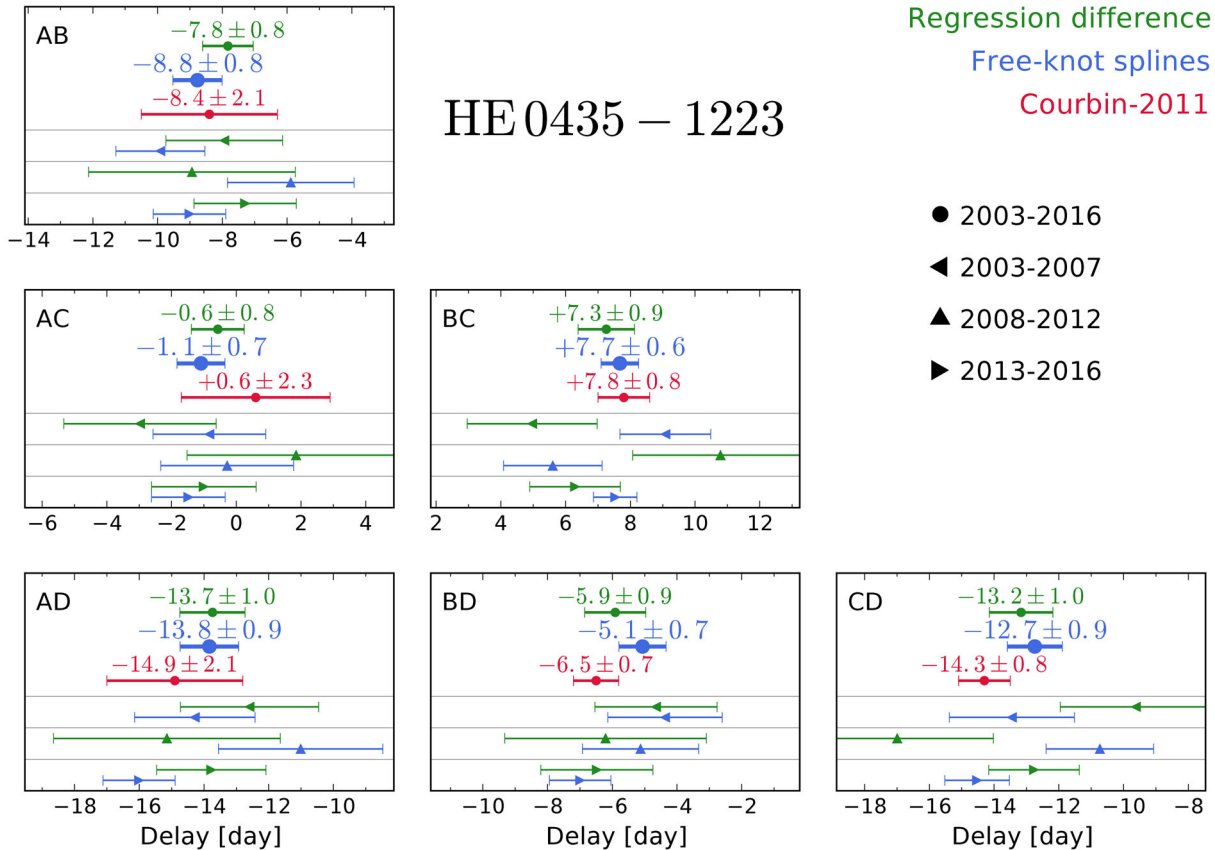
Figure 3. Time delays for the six pairs of quasar images, as indicated in top-left corner of each panel. In each panel, we show the time-delay measurement along with the 1σ error bar using our two best curve-shifting techniques, and compare with the measurement of Courbin et al. (2011). We also show the result of measurements carried out with the free-knot spline technique and regression difference technique when splitting the data in three continuous chunks of 4 or 5 yr each. All cosmological results in this work use the time-delay measurements from the free-knot splines (larger blue symbols on the figure).

the time-delay distance in the HE 0435−1223 system. The lens modelling and time-delay distance determination are addressed in detail in H0LiCOW Paper IV and are only summarized here.

4.1 Principles of the measurement

The time delay Δt_{ij} between two lensed images of the same object can be written as follows:

$$\Delta t_{ij} = \frac{D_{\Delta t}}{c}\left[\frac{(\boldsymbol{\theta}_i - \boldsymbol{\beta})^2}{2} - \psi(\boldsymbol{\theta}_i) - \frac{(\boldsymbol{\theta}_j - \boldsymbol{\beta})^2}{2} + \psi(\boldsymbol{\theta}_j)\right], \qquad (1)$$

where $\boldsymbol{\theta}_i$ and $\boldsymbol{\theta}_j$ are the coordinates of the images i and j in the lens plane, $\boldsymbol{\theta}$ is the position of the lensed images on the plane of the sky, $\boldsymbol{\beta}$ is the unlensed source position and $\psi(\boldsymbol{\theta}_i)$ is the lens potential at position $\boldsymbol{\theta}_i$. The time-delay distance $D_{\Delta t}$ is defined to be the following combination of three angular diameter distances and the deflector (i.e. the lens) redshift $z_{\rm d}$: $D_{\Delta t} \equiv (1 + z_{\rm d})D_{\rm d}D_{\rm s}/D_{\rm ds}$. Here, $D_{\rm d}$, $D_{\rm s}$ and $D_{\rm ds}$ are, respectively, the angular distances between the observer and the deflector, the observer and the source and the deflector and the source. The time-delay distance is, by construction, proportional to the inverse of the Hubble constant H_0^{-1}, and is primarily sensitive to this of all cosmological parameters. A posterior probability distribution for $D_{\Delta t}$ allows us to infer a probability distribution for H_0, assuming a given cosmology.

In the case of HE 0435−1223, there are multiple galaxies at different redshifts close in projection to the strong lens system. We explicitly include these galaxies in our multilens plane lens model

in H0LiCOW Paper IV, and in doing so introduce more angular diameter distances into the problem. However, we can still form the posterior predictive distribution for the 'effective' time-delay distance defined above, and it is the latter that we use to infer cosmological parameters. All the remaining additional mass along the line of sight can also weakly focus and defocus the light rays from the source, an effect that needs to be corrected for. We model this external contribution using an external convergence term $\kappa_{\rm ext}$ that modifies the time-delay distance as follows:

$$D_{\Delta t} = \frac{D_{\Delta t}^{\rm model}}{1 - \kappa_{\rm ext}}. \qquad (2)$$

Here, $D_{\Delta t}^{\rm model}$ is the effective time-delay distance predicted by the multiplane model, and $D_{\Delta t}$ is the corrected time-delay distance we seek. Given probability density functions (PDFs) for $P(D_{\Delta t}^{\rm model})$ and $\kappa_{\rm ext}$, we can compute the PDF for $D_{\Delta t}$. In H0LiCOW Paper IV, we derive a lognormal approximation for $P(D_{\Delta t})$, and it is this that we use as a likelihood function $P(D_{\Delta t}|\boldsymbol{\theta}, H)$ for cosmological parameters $\boldsymbol{\theta}$ given a cosmological model H.

In the rest of this section, we provide a brief summary of each part of the analysis just outlined, before proceeding to the cosmological parameter inference in Section 5.

4.2 Determination of the external convergence

We use two complementary approaches to quantify the impact of the mass along the line of sight, both yielding consistent results.

4.2.1 Spectroscopy of the field

In H0LiCOW Paper II, we perform a spectroscopic identification of a large fraction of the brightest galaxies[5] located within a projected distance of 3 arcmin of the lens. This catalogue is complemented with spectroscopic data from Momcheva et al. (2015) that augment redshift measurements to projected distances of ∼15 arcmin from the lens. Based on those data, we show that, from the five galaxies located within 12 arcsec of the lens, the galaxy G1 ($z = 0.782$), closest in projection, produces the largest perturbation of the gravitational potential, and hence needs to be explicitly included in the lens models. The other galaxies are found to produce significantly smaller perturbations. On the other hand, we search for galaxy groups and clusters that would be massive enough to modify the structure of the lens potential, but find none. On the lower mass end (i.e. groups with $\sigma \leq 500$ km s^{-1}), nine group candidates are found in the vicinity of the lens. We demonstrate that none of the groups discovered are massive enough/close enough in projection to produce high-order perturbation of the gravitational lens potential (McCully et al. 2014, 2016). This is also confirmed by a weak-lensing analysis of the field of HE 0435−1223 (Tihhonova et al., in preparation)

4.2.2 Weighted galaxy number counts

In H0LiCOW Paper III, we calculate the probability distribution for the external convergence using a weighted galaxy number counts technique (Greene et al. 2013). We conduct a wide-field, broad-band optical to mid-infrared photometric survey of the field in order to separate galaxies from stars, determine the spatial distribution of galaxies around HE 0435−1223, and estimate photometric redshifts and stellar masses. We compare weighted galaxy number counts around the lens, given an aperture and flux limit, to those through similar apertures and flux limits in CFHTLenS (Heymans et al. 2012). We investigate weights that incorporate the projected distance and redshift to the lens as well as the galaxy stellar masses. The resulting number under/overdensities serve as constraints in selecting similar fields from the Millennium Simulation, and their associated κ_{ext} values, from the catalogue of Hilbert et al. (2009). We find that the resulting distribution of κ_{ext} is consistent with the typical mean density value (i.e. $\kappa_{ext} = 0$) and is robust to choices of weights, apertures, flux limits and cosmology, up to an impact of 0.5 per cent on the time-delay distance.

4.3 Mass modelling

In H0LiCOW Paper IV, we perform our lens modelling using GLEE, a software package developed by A. Halkola and S. H. Suyu (Suyu & Halkola 2010; Suyu et al. 2012). Our fiducial mass model for the lens galaxy is a singular power-law elliptical mass distribution with external shear. We explicitly include the closest line of sight perturbing galaxy in the lens model (G1; see fig. 3 of H0LiCOW Paper IV), using the full multiplane lens equation to account for its effects. We also include in an extended modelling four other nearby perturbing galaxies to check their impact. Because the perturbers are at different redshifts, there is no single time-delay distance that

---

[5] The completeness of the spectroscopic identification depends on the distance to the lens and limiting magnitude, see fig. 3 of H0LiCOW Paper II. For example, 60 per cent (80 per cent) of the galaxies brighter than $i \sim 22$ mag ($i \sim 21.5$ mag) have a measured spectroscopic redshift within a radius of 3 arcmin (2 arcmin) of the lens.

can be clearly defined. Instead, we vary H_0 directly in our models and then use this distribution to calculate an effective time-delay distance, where the angular diameter distances D_d and D_s are calculated using the redshift of the main deflector, $z_d = 0.454$. We assume a fiducial cosmology, $\Omega_m = 0.3$, $\Omega_\Lambda = 0.7$ and $w = -1$ in this modelling procedure, but we find that allowing these cosmological parameters to vary has a negligible (<1 per cent) effect on the resulting effective time-delay distance distribution.

The MSD – the invariance to the lensed images under addition of a uniform mass sheet to our mass model combined with a rescaling of the source plane coordinates – can affect the inferred time delays, and may limit the effectiveness of time delays in constraining cosmology (e.g. Schneider & Sluse 2013, 2014). We have shown in previous work that including the central velocity dispersion of the main galaxy in the lens modelling minimizes the effect of the MSD (see fig. 4 of Suyu et al. 2014). In the case of HE 0435−1223, we measure $\sigma = 222 \pm 15$ km s^{-1} using Keck I spectroscopy. We also show that mass models that go beyond the elliptically-symmetric power-law profile, and that are better physically justified, fit our data equally well yet lead to the same cosmological inference. As in Suyu et al. (2014), the H0LiCOW Paper IV tests both power law and a composite model with a baryonic component and an NFW dark matter halo. We also note that the completely independent models of Birrer, Amara & Refregier (2016) confirm the findings of Suyu et al. (2014).

We model the images of the lensed source simultaneously in three *HST* bands: ACS/*F555W*, ACS/*F814W* and WFC3/*F160W*. The lensed quasar images are modelled as point sources convolved with the PSF. The extended, unlensed image of the host galaxy of the quasar is modelled separately on a pixel grid with curvature regularization (see e.g. Suyu et al. 2006). Our constraints on the model include the positions of the quasar images, the measured time delays and the surface brightness pixels in each of the three bands. Model parameters of the lens are explored through Markov Chain Monte Carlo (MCMC) sampling, while the Gaussian posterior PDF for the source pixel values is characterized using standard linear algebra techniques (e.g. Suyu et al. 2006).

During our modelling procedure, we iteratively update the PSFs using the lensed AGN images themselves in a manner similar to Chen et al. (2016), and we use these corrected PSFs in our final models (for more details, see Suyu et al., in preparation). We conduct multiple robustness tests to account for various systematic uncertainties in the modelling. We vary our choice of modelling regions and use various weights for each pixel. We use various assumptions for the light profiles fits of the lens galaxy and we model the lens using alternative mass models, comparing the use of power-law profiles and chameleon profiles. We also explicitly include the five nearest perturbing galaxies into our modelling. All the models are given a similar weight, reflecting the possible choices available through the analysis, and are combined together to yield a single posterior PDF for $D_{\Delta t}$. Fig. 9 of H0LiCOW Paper IV presents the individual and combined posterior distributions, highlighting on one hand the relatively good agreement between the models, and on the other hand the need to consider a sufficiently flexible model to fully take into account as many sources of systematics as possible.

4.4 Blinding methodology and unblinded results

A key element of our analysis is that it is carried out blindly with respect to the inference of cosmological parameters. This blindness is crucial in order to avoid unconscious confirmation bias. In practice, blindness is built into our measurement in the following manner. All

the individual measurements and modelling efforts in H0LiCOW
Paper IV are carried out without any knowledge of the effects of
specific choices on the resulting cosmology. In some cases, this
blindness is trivial to achieve; for example, the measurement of ve-
locity dispersion was carried out and finalized independently from
the cosmological inference, and the connection between the two is
significantly complex and indirect that the person carrying out the
velocity dispersion measurement effectively had no way to deter-
mine how that could affect cosmological parameters. In other cases,
building on the procedure established by our previous analysis of
RXJ1131−1231 (Suyu et al. 2013), blindness was achieved by only
using plotting codes that offset every posterior probability distri-
bution for time-delay distance and cosmological parameters by a
constant (such as the median value of each marginal distribution),
and thus never revealing the actual measurements to the investi-
gators until the time of unblinding (see discussion in H0LiCOW
Paper IV).

All of our analysis and visualization tools were developed and
tested using simulated quantities. No modifications were allowed
after the official unblinding, making the unblinding step irreversible.
The official unblinding was originally scheduled for 2016 June 2
during a teleconference open to all the co-authors. Additional tests
were suggested during this meeting. As a result, the analysis was
kept blind for another two weeks and the final unblinding happened
during a teleconference starting at 6 AM UT on 2016 June 16 and
was audio recorded by LVEK without others knowing until the
end of the teleconference. The results presented in the next sec-
tion are the combination of the blind measurements obtained for
HE 0435−1223 and RXJ1131−1231,[6] and the not-blind measure-
ments obtained by our team for the first system B1608+656.

5 JOINT COSMOGRAPHY ANALYSIS

Cosmic microwave background (CMB) experiments provide a
model-dependent value of the Hubble constant, H_0, which appear
to be in some tension with methods based on standard rulers and
standard candles. In a flat-ΛCDM universe, the significance of the
tension between the most recent values from Planck (Planck Col-
laboration XIII 2016a) and the direct measurement from Cepheids
and Type Ia Supernovae (Riess et al. 2016) is 3.3σ. Either this
tension is due, at least in part, to systematics in the measure-
ments (as suggested by e.g. Efstathiou 2014), or it is caused by
new physics beyond the predictions of flat ΛCDM. Several authors
discuss the possibility of relaxing the usual assumptions about cos-
mological parameters as a way to reduce the tension (e.g. Salvatelli
et al. 2013; Heavens, Jimenez & Verde 2014; Di Valentino,
Melchiorri & Silk 2016). Possible assumptions include, for exam-
ple, that we live in a non-flat universe ($\Omega_k \neq 0$), that the dark energy
equation of state is not a cosmological constant ($w \neq -1$), that the
sum of the neutrino masses is larger than predicted by the stan-
dard hierarchy scenario ($\Sigma m_\nu > 0.06$ eV), and/or that the effective
number of relativistic neutrino species may differ from its assumed
value in the standard model ($N_{eff} \neq 3.046$). Given the above, it is
important to consider a range of plausible extended cosmological
models when investigating the information that can be gained from

any specific cosmological probe (see e.g. Collett & Auger 2014;
Giusarma et al. 2016).

In this context, we present below our inference of the cosmo-
logical parameters obtained using the time-delay distance measure-
ments of the strongly lensed quasars B1608+656, WFI2033−4723
and HE 0435−1223. After making sure that their individual results
are consistent with each other, we present our cosmological infer-
ence using all three systems jointly, referred as 'TDSL' for 'Time
Delay Strong Lensing'. We then combine TDSL with the *WMAP*
Data Release 9 (hereafter '*WMAP*'; Bennett et al. 2013; Hinshaw
et al. 2013) and with the Planck 2015 Data Release[7] (Planck Collab-
oration XIII 2016a, hereafter 'Planck'). When available, we also use
the combination of Planck data with Planck measurements of CMB
weak-lensing (hereafter 'CMBL'; Planck Collaboration XV 2016b),
with baryon acoustic oscillation surveys at various redshifts (here-
after BAO; Percival et al. 2010; Beutler et al. 2011; Blake et al. 2011;
Anderson et al. 2012; Padmanabhan et al. 2012) and with the data
of the Joint Lightcurve Analysis of Supernovae (hereafter 'JLA';
Betoule et al. 2013). The latter two data sets are described in detail
in section 5.2 of Planck Collaboration XVI et al. (2014) and sec-
tion 5.3 of Planck Collaboration XIII (2016a), respectively. Note
that when possible, we do not combine the cosmological probes
other than TDSL ourselves, but instead we use the combined results
published and provided by the Planck team.[8]

We follow the importance sampling approach suggested by Lewis
& Bridle (2002) and employed by Suyu et al. (2010, 2013), re-
weighting the *WMAP* and Planck posterior samples with the TDSL
likelihoods from the analyses of B1608+656 (Suyu et al. 2010),
RXJ1131−1231 (Suyu et al. 2014) and HE 0435−1223 (H0LiCOW
Paper IV), for the set cosmological models described in Table 2.

We consider both (i) 'uniform' cosmologies, with only a few
variable cosmological parameters with uniform priors in order to get
constraints from TDSL alone, and (ii) cosmologies extended beyond
ΛCDM where we combine the TDSL likelihoods with other probes.
When comparing two cosmological parameter inferences, we use
the following terminology. When two results differ by less than 1σ,
we consider that they are 'consistent'; in the 1σ–2σ range they are
in 'mild tension'; in the 2σ–3σ range they are in 'tension'; above
3σ, they are in 'significant tension'. If a cosmological parameter
inference follows a non-Gaussian distribution, we use '1σ' to refer
to the width of the distribution between its 50th and 16th percentiles
if the comparison is made towards a lower value, and between its
50th and 84th percentiles if the comparison is made towards a higher
value. In a comparison, the σ values always refer to those belonging
to the distribution that includes TDSL.

5.1 Cosmological inference from strong lensing alone

We first present our values for the cosmological parameters that
can be inferred from TDSL alone. We use the time-delay distance
likelihoods analytically expressed with a skewed lognormal distri-
bution:

$$P(D_{\Delta t}) = \frac{1}{\sqrt{2\pi}(x - \lambda_D)\sigma_D} \exp\left[-\frac{(\ln(x - \lambda_D) - \mu_D)^2}{2\sigma_D^2}\right], \quad (3)$$

---

[6] The time-delay distance measurement of RXJ1131−1231 from Suyu et al.
(2014) that includes a composite model for the lens was not blind, whereas
the first measurement of this same lens from Suyu et al. (2013) was done
blindly.

[7] We use the Planck chains designated by 'plikHM_TT_lowTEB' that uses
the baseline high-L Planck power spectra and low-L temperature and LFI
polarization.

[8] http://pla.esac.esa.int/pla/#cosmology

Table 2. Description of the cosmological models considered in this work. *WMAP* refers to the constraints given in the *WMAP* Data Release 9. Planck refers either to the constraints from Planck 2015 Data Release alone, or combined with CMBL, BAO and/or JLA. See Section 5 for details.

Model name	Description
UH_0	Flat $-\Lambda$ CDM cosmology
	$\Omega_m = 1 - \Omega_\Lambda = 0.32$
	H_0 uniform in [0, 150]
UΛCDM	Flat $-\Lambda$ CDM cosmology
	$\Omega_m = 1 - \Omega_\Lambda$
	H_0 uniform in [0, 150]
	Ω_m uniform in [0, 1]
UwCDM	Flat $-w$CDM cosmology
	H_0 uniform in [0, 150]
	Ω_{de} uniform in [0, 1]
	w uniform in $[-2.5, 0.5]$
UoΛCDM	Non $-$ flat $-\Lambda$ CDM cosmology
	$\Omega_m = 1 - \Omega_\Lambda - \Omega_k > 0$
	H_0 uniform in [0, 150]
	Ω_Λ uniform in [0, 1]
	Ω_k uniform in $[-0.5, 0.5]$
oΛCDM	Non $-$ flat $-\Lambda$ CDM cosmology
	WMAP/Planck for $\{H_0, \Omega_\Lambda, \Omega_m\}$
	$\Omega_k = 1 - \Omega_\Lambda - \Omega_m$
N$_{eff}\Lambda$CDM	Flat $-\Lambda$ CDM cosmology
	WMAP/Planck for $\{H_0, \Omega_\Lambda, N_{eff}\}$
m$_\nu\Lambda$CDM	Flat $-\Lambda$ CDM cosmology
	WMAP/Planck for $\{H_0, \Omega_\Lambda, \Sigma m_\nu\}$
wCDM	Flat $-w$CDM cosmology
	Planck for $\{H_0, w, \Omega_{de}\}$
N$_{eff}$m$_\nu\Lambda$CDM	Flat $-\Lambda$ CDM cosmology
	Planck for $\{H_0, \Omega_\Lambda, \Sigma m_\nu, N_{eff}\}$
owCDM	Open Λ CDM cosmology
	Planck for $\{H_0, \Omega_{de}, \Omega_k, w\}$

where $x = D_{\Delta t}/(1 \text{ Mpc})$. We recall in Table 3 the lens and source redshifts of the three strong lenses as well as the parameters μ_D, σ_D and λ_D describing their respective time-delay distance distributions.

5.1.1 Combination of three lenses

Before carrying out a joint analysis of our three lens systems, we first perform a quantitative check that our three lenses can be combined without any loss of consistency. For that purpose, we compare their time-delay distance likelihood functions in the full cosmological parameter space, and measure the degree to which they overlap. Following Marshall, Rajguru & Slosar (2006) and Suyu et al. (2013), we compute the Bayes factor F, or evidence ratio, in favour of a simultaneous fit of the lenses using a common set of cosmological parameters. When comparing three data sets d_1, d_2 and d_3, we can either assume the hypothesis H^{global} that they can be represented using a common global set of cosmological parameters, or the hypothesis H^{ind} that at least one data set is better represented using

another independent set of cosmological parameters. We stress that this latter model would make sense if there was a systematic error present that led to a vector offset in the inferred cosmological parameters. To parametrize this offset vector with no additional information would take as many nuisance parameters as there are dimensions in the cosmological parameter space; assigning uninformative uniform prior PDFs to each of the offset components is equivalent to using a complete set of independent cosmological parameters for the outlier 5 data set.

The Bayes factor, that makes the H^{global} hypothesis F times more probable than H^{ind} can be computed as follows:

$$F = \frac{P(d_1, d_2, d_3 | H^{global})}{P(d_1 | H^{ind}) P(d_2 | H^{ind}) P(d_3 | H^{ind})}. \quad (4)$$

A Bayes factor F significantly larger than 1 indicates that the considered data sets can be consistently combined. In the present case, considering three lenses with known time-delay distance likelihoods L_1, L_2 and L_3, the Bayes factor becomes

$$F_{1\cup2\cup3} = \frac{\langle L_1 L_2 L_3 \rangle}{\langle L_1 \rangle \langle L_2 \rangle \langle L_3 \rangle}, \quad (5)$$

where angle brackets denote averages over our ensembles of prior samples. We can also compare the likelihoods pair by pair (1-versus-1) as in equation 27 of Suyu et al. (2013) and then combine each pair with the third likelihood (2-versus-1):

$$F_{12\cup3} = \frac{\langle L_1 L_2 L_3 \rangle}{\langle L_1 L_2 \rangle \langle L_3 \rangle}. \quad (6)$$

This last equation allows us to check that the lenses can also be well combined pair-wise, and that none of them is inconsistent with the two others considered together. We compute the Bayes Factors $F_{1\cup2\cup3}$ and all the possible 1-versus-1 and 2-versus-1 permutations in the uniform cosmologies UH_0, UΛCDM, UwCDM and UoΛCDM. We find that all the combinations are in good agreement, the only exception being for the pair B1608+656 $\cup$ RXJ1131$-$1231, which is only marginally consistent in the UoΛCDM cosmology ($F_{1\cup2}=1.1$). Considering the likelihoods individually, the three lenses are in excellent agreement, with a Bayes Factor $F_{1\cup2\cup3} = 21.3$ in UH_0, $F_{1\cup2\cup3} = 14.2$ in UΛCDM, $F_{1\cup2\cup3} = 18.9$ in UwCDM and $F_{1\cup2\cup3} = 10.8$ in UoΛCDM. We conclude that the time-delay likelihoods of our three lenses can be combined without any loss of consistency.

5.1.2 Constraints in uniform cosmologies

Fig. 4 presents the marginalized posterior PDF for H_0 in the cosmological models using uniform priors. Our baseline model, UH_0, has a uniform prior on H_0 in the range [0, 150] km s^{-1} Mpc^{-1}, a matter density fixed at $\Omega_m = 0.32$ from the most recent Planck results (Planck Collaboration XIII 2016a), zero curvature $\Omega_k = 0$ and consequently a fixed cosmological constant. This model has only one free parameter. From left to right in the figure, we present this UH_0 cosmology, and then three models that have two or three

Table 3. Parameters of the three strong lenses used in our analysis. μ_D, σ_D and λ_D are related to the analytical fit of the time-delay distance probability function (see equation 3).

| Name	Reference	z_d	z_s	μ_D	σ_D	λ_D
B1608+656	Suyu et al. (2010)	0.6304	1.394	7.0531	0.228 24	4000.0
RXJ1131$-$1231	Suyu et al. (2014)	0.295	0.654	6.4682	0.205 60	1388.8
HE 0435$-$1223	H0LiCOW Paper IV	0.4546	1.693	7.5793	0.103 12	653.9
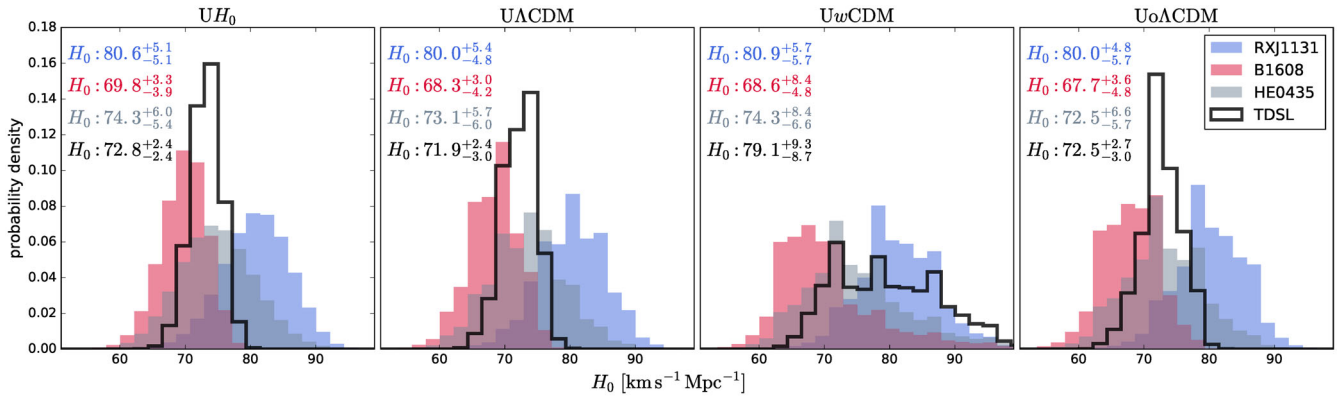
Figure 4. Marginalized posterior probability distributions for H_0 in the UH_0, UΛCDM, UwCDM and UoΛCDM cosmologies using the constraints from the three strong lenses B1608+656, RXJ1131−1231 and HE 0435−1223. The overlaid histograms present the distributions for each individual strong lens (ignoring the other two data sets), and the solid black line corresponds to the distribution resulting from the joint inference from all three data sets (TDSL). The quoted values of H_0 in the top-left corner of each panel are the median, 16th and 84th percentiles.

free parameters (H_0 plus one or two others): the UΛCDM cosmology where we allow Ω_m to vary with uniform prior; the UwCDM cosmology with a free Ω_{de} and a free time-independent dark energy equation of state w, both with uniform priors; and finally the UoΛCDM cosmology, that relaxes the constraint on the curvature Ω_k and allows both this and Ω_Λ to vary with uniform priors. Table 2 summarizes the constraints and priors for these four models. We quote in each panel the corresponding median and 1σ uncertainties of H_0. In the UH_0 cosmology, combining the three lenses yields a value $H_0 = 72.8 \pm 2.4\,\mathrm{km\,s^{-1}\,Mpc^{-1}}$, with 3.3 per cent precision. When relaxing the constraint on Ω_m in UΛCDM (and thus being completely independent of any other measurement), we obtain $H_0 = 71.9^{+2.4}_{-3.0}\,\mathrm{km\,s^{-1}\,Mpc^{-1}}$, with 3.8 per cent precision. These two estimates are, respectively, 2.5σ and 1.7σ higher than the most recent Planck measurement in a flat-ΛCDM universe ($H_0 = 66.93 \pm 0.62\,\mathrm{km\,s^{-1}\,Mpc^{-1}}$; Planck Collaboration XIII 2016a), in excellent agreement with the most recent results using distance ladders ($H_0 = 73.24 \pm 1.74\,\mathrm{km\,s^{-1}\,Mpc^{-1}}$; Riess et al. 2016), and compatible with other local estimates (see e.g. Bonamente et al. 2006; Freedman et al. 2012; Sorce, Tully & Courtois 2012; Gao et al. 2016). Whether the tension between the local and cosmological measurements of H_0 comes from systematic errors or hints at new physics beyond flat ΛCDM is currently a hot topic of discussion in the community (see e.g. Efstathiou 2014; Rigault et al. 2015; Spergel, Flauger & Hložek 2015; Addison et al. 2016; Di Valentino, Melchiorri & Silk 2016; Planck Collaboration XIII 2016a; Riess et al. 2016, and references therein).

Intriguingly, we note that the H_0 values yielded by each system individually get larger for lower lens redshifts. So far, we cannot state if this comes from a simple statistical fluke, an unknown systematic error or hints towards an unaccounted physical property. The addition of two more lenses from the H0LiCOW sample will certainly help us in that regard.

Fig. 5 presents the two-dimensional 95 per cent credible regions of the cosmological parameters in the UwCDM, UoΛCDM and UΛCDM cosmologies for each lens individually and for their combination (TDSL). TDSL is primarily sensitive to H_0, and the tilt in the $H_0 - \Omega_\Lambda$, $H_0 - w$ and $H_0 - \Omega_k$ planes illustrates its weak sensitivity to the dark energy density, dark energy equation of state and curvature density, respectively. TDSL alone agrees both with a flat universe and a cosmological constant, although on the latter the credible region extends deeply into the phantom dark energy domain ($w < -1$). In the UwCDM cosmology, the correlation be-
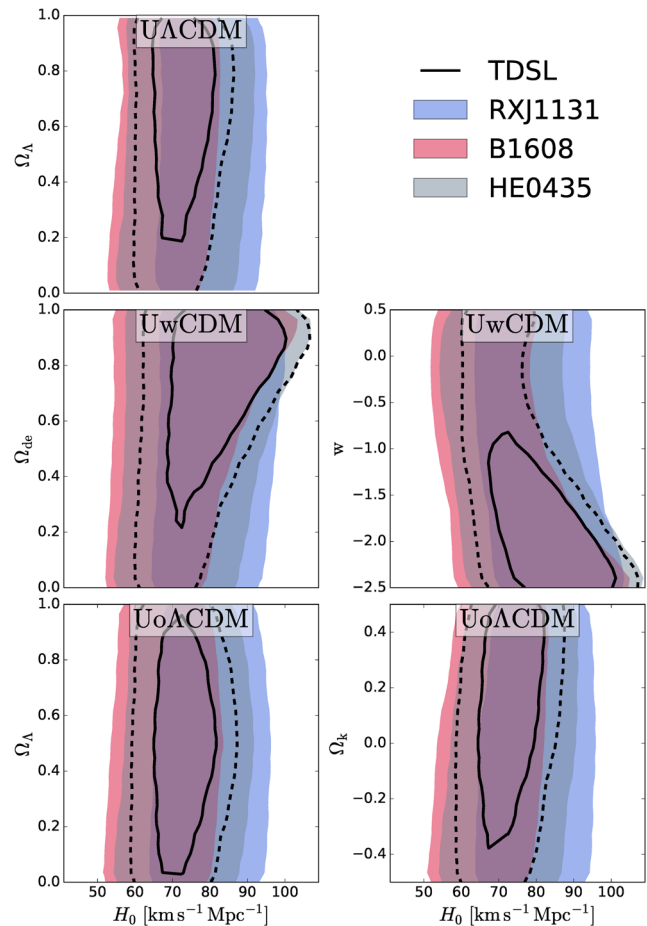
Figure 5. Comparison of the three strong lenses in the UΛCDM (top), UwCDM (middle) and UoΛCDM (bottom) cosmologies. The coloured overlays delimit the 95 per cent credible region for B1608+656, RXJ1131−1231 and HE 0435−1223. The solid and dashed black lines draw the contours of the 68.3 and 95 per cent credible regions, respectively, for the combination of the three lenses.

tween H_0 and w is more prominent than in the other models, leading to a larger dispersion of the H_0 distribution in the corresponding panel of Fig. 4. This dispersion is more prominent for values of $w < -1$, since in such cases the variation of the density of dark

Table 4. Summary of the cosmological parameters constraints for the models detailed in Table 2. H_0 units are km s^{-1} Mpc^{-1}, Σm_ν units are eV. The quoted values are the median, 16th and 84th percentiles, except for Σm_ν where we quote the 95 per cent upper bound of the probability distribution. The empty slots occur when no prior samples are provided by the Planck team.

	UH_0	$U\Lambda$CDM		UwCDM			$Uo\Lambda$CDM		
	H_0	H_0	Ω_Λ	H_0	Ω_{de}	w	H_0	Ω_Λ	Ω_k
TDSL	$72.8^{+2.4}_{-2.4}$	$71.9^{+2.4}_{-3.0}$	$0.62^{+0.24}_{-0.35}$	$79.1^{+9.3}_{-8.7}$	$0.72^{+0.19}_{-0.34}$	$-1.79^{+0.94}_{-0.49}$	$72.5^{+2.7}_{-3.0}$	$0.51^{+0.28}_{-0.30}$	$0.1^{+0.3}_{-0.3}$

	$o\Lambda$CDM				wCDM		
	H_0	Ω_m	Ω_Λ	Ω_k	H_0	Ω_{de}	w
TDSL+*WMAP*	$73.0^{+2.3}_{-2.5}$	$0.25^{+0.02}_{-0.05}$	$0.74^{+0.02}_{-0.02}$	$0.005^{+0.005}_{-0.005}$	$76.5^{+4.6}_{-3.9}$	$0.76^{+0.02}_{-0.02}$	$-1.24^{+0.16}_{-0.20}$
TDSL+Planck (1)	$69.2^{+1.4}_{-2.2}$	$0.30^{+0.02}_{-0.02}$	$0.70^{+0.01}_{-0.01}$	$0.003^{+0.004}_{-0.006}$	$79.0^{+4.4}_{-4.2}$	$0.77^{+0.02}_{-0.03}$	$-1.38^{+0.14}_{-0.16}$
(1)+BAO	$68.0^{+0.7}_{-0.7}$	$0.31^{+0.01}_{-0.01}$	$0.69^{+0.01}_{-0.01}$	$0.001^{+0.003}_{-0.003}$	$69.6^{+1.8}_{-1.7}$	$0.70^{+0.01}_{-0.01}$	$-1.08^{+0.07}_{-0.08}$
(1)+BAO+JLA	$68.1^{+0.7}_{-0.7}$	$0.31^{+0.01}_{-0.01}$	$0.69^{+0.01}_{-0.01}$	$0.001^{+0.003}_{-0.003}$	$68.8^{+1.0}_{-1.0}$	$0.70^{+0.01}_{-0.01}$	$-1.04^{+0.05}_{-0.05}$

	$N_{eff}\Lambda$CDM			$m_\nu\Lambda$CDM		
	H_0	Ω_Λ	N_{eff}	H_0	Ω_Λ	Σm_ν (eV)
TDSL+*WMAP*	$73.2^{+2.2}_{-2.4}$	$0.72^{+0.02}_{-0.03}$	$3.86^{+0.73}_{-0.71}$	$70.7^{+1.9}_{-1.9}$	$0.73^{+0.02}_{-0.02}$	≤ 0.393
TDSL+Planck (1)	$71.0^{+2.0}_{-2.0}$	$0.71^{+0.01}_{-0.01}$	$3.45^{+0.23}_{-0.24}$	$68.1^{+1.1}_{-1.2}$	$0.70^{+0.01}_{-0.02}$	≤ 0.199
(1)+BAO	$69.6^{+1.4}_{-1.3}$	$0.70^{+0.01}_{-0.01}$	$3.34^{+0.21}_{-0.21}$	$67.9^{+0.6}_{-0.6}$	$0.69^{+0.01}_{-0.01}$	≤ 0.182
(1)+BAO+CMBL				$67.9^{+0.6}_{-0.7}$	$0.69^{+0.01}_{-0.01}$	≤ 0.216

	$N_{eff}m_\nu\Lambda$CDM				owCDM			
	H_0	Ω_Λ	N_{eff}	Σm_ν (eV)	H_0	Ω_{de}	Ω_k	w
TDSL+Planck (1)	$70.8^{+2.0}_{-2.1}$	$0.71^{+0.02}_{-0.02}$	$3.44^{+0.24}_{-0.24}$	≤ 0.274	$88.4^{+5.9}_{-7.2}$	$0.83^{+0.02}_{-0.03}$	$-0.010^{+0.003}_{-0.003}$	$-2.10^{+0.34}_{-0.41}$
(1)+CMBL	$70.8^{+2.1}_{-2.1}$	$0.71^{+0.02}_{-0.02}$	$3.44^{+0.25}_{-0.24}$	≤ 0.347	$77.9^{+5.0}_{-4.2}$	$0.77^{+0.03}_{-0.03}$	$-0.003^{+0.004}_{-0.004}$	$-1.37^{+0.18}_{-0.23}$
(1)+BAO+CMBL					$70.0^{+2.1}_{-1.7}$	$0.71^{+0.02}_{-0.02}$	$-0.000^{+0.004}_{-0.003}$	$-1.07^{+0.09}_{-0.10}$

energy becomes larger at low redshifts. Since our measurements are performed at the redshift of the lenses we observe, going back to redshift zero and H_0 produces the degeneracy with w.

This highlights the fact that our cosmological inferences in this cosmology are more sensitive to the prior range we choose. Thus, the resulting parameter values must be considered as indicative of a trend rather than as absolute measurements. We summarize our values for H_0, Ω_k, w and Ω_m from TDSL alone in the top section of Table 4.

5.2 Constraining cosmological models beyond ΛCDM

We now investigate how strong lensing can help constrain cosmological models beyond standard flat ΛCDM, when combined with other cosmological probes. We demonstrated in Section 5.1 and Fig. 5 that TDSL is only weakly dependent on the matter density, the dark energy density, the dark energy equation of state and the curvature. However, the cosmological parameter degeneracies for TDSL are such that the combination of TDSL with other probes can rule out large areas of parameter space. Following the motivations presented in Planck Collaboration XIII (2016a) for extensions to the base ΛCDM model, we present in the following a selection of models where we combine TDSL with the results from *WMAP*, Planck, Planck+BAO, Planck+BAO+CMBL

and Planck+BAO+JLA when available. Figs 6 and 7 present the results. Note that we have smoothed the contours of the credible regions after importance sampling with a Gaussian filter due to the sparsity of the *WMAP* and Planck MCMC chains, checking that the 95 per cent credible regions do indeed contain approximately 95 per cent of the importance weight.

5.2.1 One-parameter extensions

We first consider one-parameter extensions to the standard model, where we relax the constraints on one additional cosmological parameter from flat ΛCDM. We present in Fig. 6 the two-dimensional marginalized parameter space for a selection of cosmological models for which the impact of TDSL is the most meaningful.

In the oΛCDM model, we consider a non-flat universe with $\Omega_k \neq 0$. In the $N_{eff}\Lambda$CDM model, we consider a variable effective number of relativistic neutrino species N_{eff} with a fixed total mass of neutrinos $\Sigma m_\nu = 0.06$ eV. In the $m_\nu\Lambda$CDM model, we consider a variable Σm_ν with a fixed $N_{eff} = 3.046$. Finally, in the wCDM model we consider a time-invariant dark energy equation of state w. A detailed description of these models is given in Table 2.

For each probe, or combination of probes, we draw the 95 per cent credible region contours as coloured lines. When combined with TDSL, the updated credible region is displayed as a filled area.
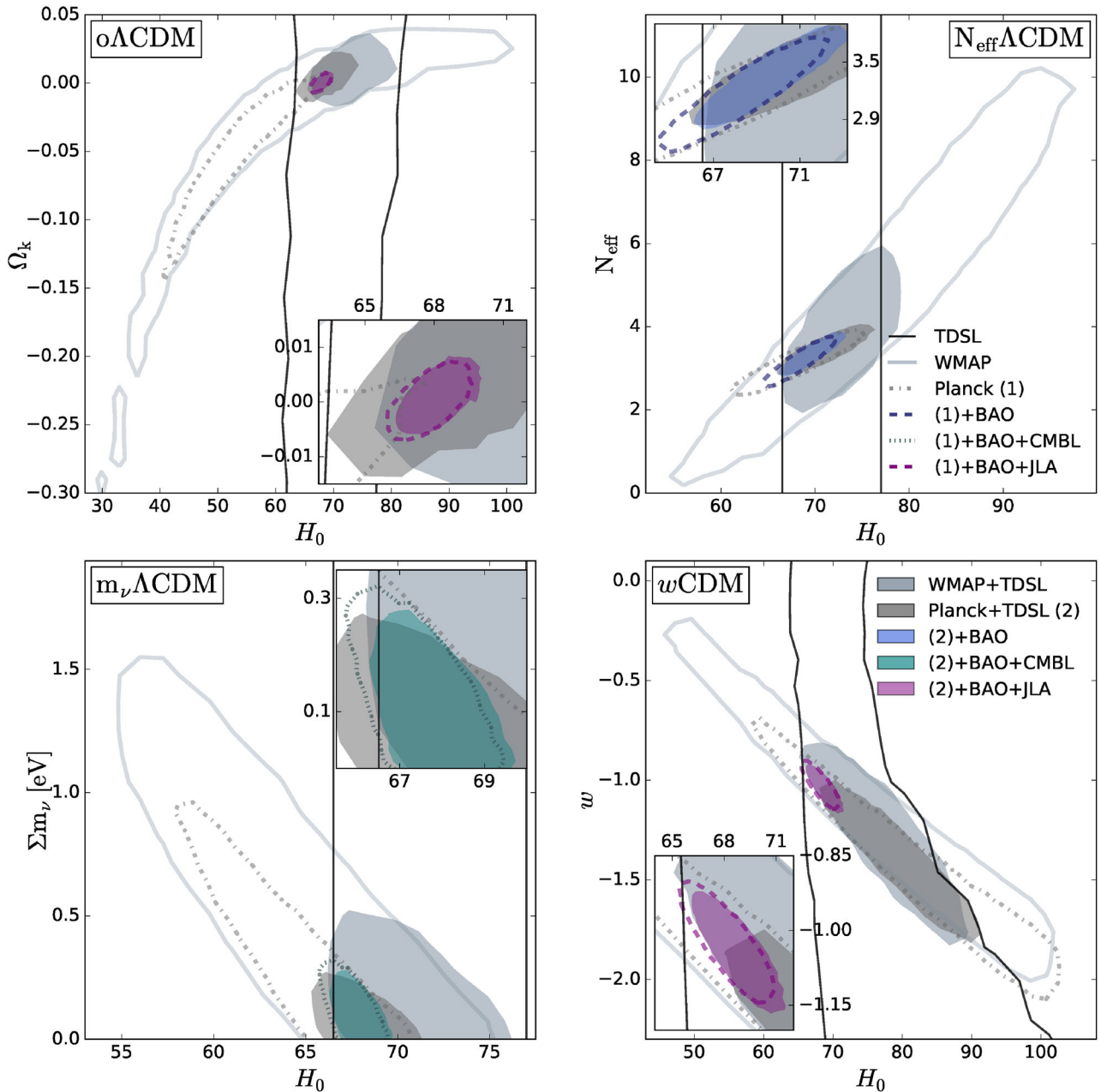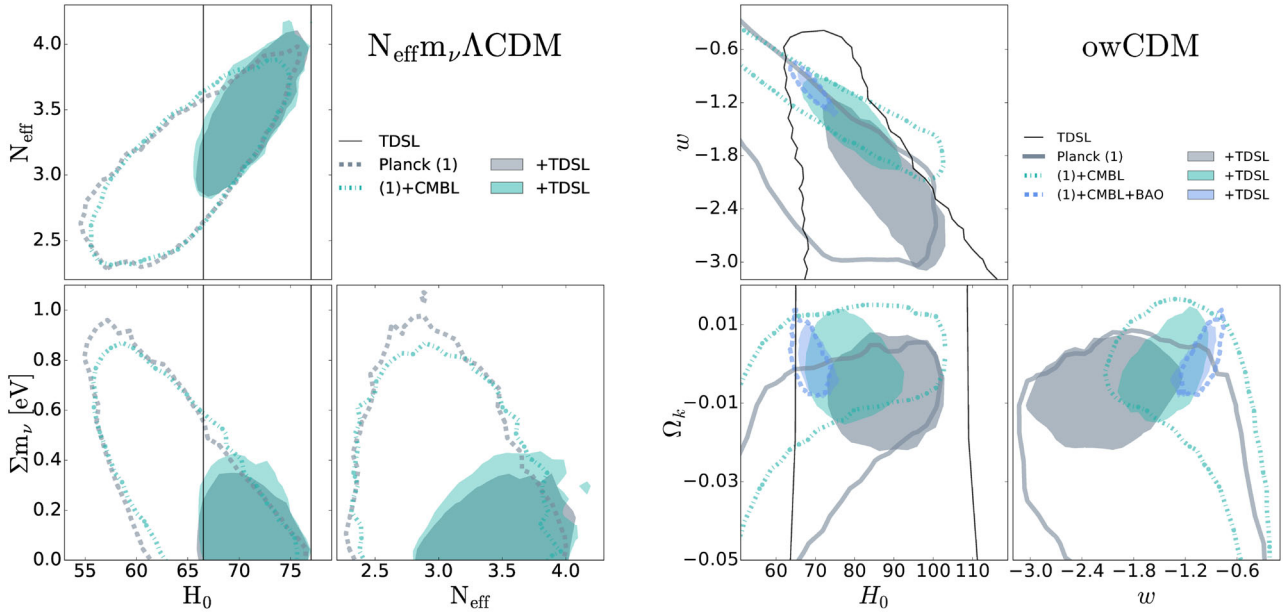
Figure 6. Cosmological constraints in one-parameter extensions to ΛCDM. We consider a non-flat universe with variable curvature Ω_k (top-left), a variable effective number of relativistic neutrino species N_{eff} (top-right), a variable total mass of neutrino species Σm_ν (bottom-left, in eV) and a variable time-invariant dark energy equation of state w (bottom-right). The filled regions and coloured lines delimit the marginalized 95 per cent credible regions (consistently smoothed due to the sparsity of the samples from the available MCMC chains) with and without the constraints from TDSL, respectively. The different colours represent the constraints from *WMAP*, Planck, Planck+CMBL, Planck+BAO, Planck+CMBL+BAO and Planck+BAO+JLA. The solid black lines delimit the 95 per cent credible region for TDSL alone in the corresponding uniform cosmology with no additional information.

When importance sampling using priors based on other probes, it is important to verify that the respective constraints in the parameter space overlap. If they do not, the probes considered may not be efficiently combined. With this in mind, we plot in each cosmology the 95 per cent credible region for TDSL only (and uniform priors) as thin solid black lines. We note that in all one-parameter extensions presented here, the 2D marginalized TDSL and Planck 95 per cent credible regions at least partially overlap, although in the oΛCDM and m$_\nu\Lambda$CDM cosmologies, the 1D marginalized posterior mean value for H_0 from TDSL lies outside the 95 per cent credible region

of Planck. We consider the overlaps to be sufficient to justify our importance sampling TDSL with Planck, but emphasize that the joint constraints must be interpreted cautiously. *WMAP* and Planck constraints are in agreement with each other, this being at least partly due to the large parameter space covered in the credible region of *WMAP*. This also results in a much wider overlap with the TDSL 95 per cent credible regions.

We summarize our inferred values for H_0 and other cosmological parameters of each cosmology in Table 4. In the oΛCDM cosmology, both *WMAP*+TDSL and Planck+TDSL are consistent with a

Figure 7. Cosmological constraints in two-parameter extensions to ΛCDM. We consider a flat universe with variable effective number of relativistic neutrino species $N_{\rm eff}$ and total mass of neutrinos Σm_ν (left), and an open universe with variable dark energy equation of state parameters w (right). The coloured lines and filled areas are the same as in Fig. 6, and show marginalized 95 per cent credible regions. The TDSL contours in the owCDM cosmology are computed using uniform priors on $\Omega_{\rm k}$ [-0.5, 0.5] and w [-2.5, 0.5].

flat universe. The constraints on $\Omega_{\rm k}$ from Planck+TDSL are approximately twice as large as those from Planck+BAO+JLA. In the $m_\nu\Lambda$CDM cosmology, the upper bound of the sum of the neutrino masses Σm_ν from *WMAP*+TDSL is approximately twice as large as the prediction from Planck+TDSL. The addition of TDSL lowers the upper bound from Planck+BAO by about 5 per cent. The joint constraint from Planck+BAO+TDSL yields $\Sigma m_\nu \leq 0.182$ eV with 95 per cent probability. In the $N_{\rm eff}\Lambda$CDM cosmology, both *WMAP*+TDSL and Planck+TDSL suggest an effective number of relativistic neutrino species higher than the standard cosmological prediction of $N_{\rm eff} = 3.046$. The Planck+TDSL value is similar in precision to Planck+BAO, yet the two values are in mild tension, the former being 1.3σ higher. The combination of Planck+BAO+TDSL yields $N_{\rm eff} = 3.34 \pm 0.21$, also in mild tension with the standard cosmological prediction. In the wCDM cosmology, Planck+TDSL points towards $w = -1.38^{+0.14}_{-0.16}$, a result in tension with a cosmological constant ($w = -1$) at a 2.3σ level. This value is lower than other values for phantom dark energy reported in the literature (see e.g. Freedman et al. 2012; Collett & Auger 2014). With *WMAP*+TDSL we find $w = -1.24^{+0.16}_{-0.20}$, consistent with the previous measurement from our group using just B1608+656 and RXJ1131−1231 combined with *WMAP* of $w = -1.14^{+0.17}_{-0.20}$ (Suyu et al. 2013).

5.2.2 Two-parameter extensions

We now consider cosmological models where we relax the priors on two cosmological parameters from flat ΛCDM. Following the discussion of Section 5.2.1 where we noted that the individual TDSL and Planck 95 per cent credible regions only partially overlap, we consider here two cosmological models that reduce the tension between these two probes. First, we consider the $N_{\rm eff}m_\nu\Lambda$CDM model, where both the effective number of relativistic neutrino species $N_{\rm eff}$ as well as their total mass Σm_ν are allowed to vary. Secondly, we consider the owCDM model where we relax the constraints

on both the curvature, $\Omega_{\rm k}$, and the dark energy equation of state parameter w simultaneously. For the owCDM model, the Planck team does not publicly provide MCMC chains. We therefore generate additional chains using the publicly available Planck cosmological likelihood function, *plik* (Planck Collaboration XVIII 2016c). Temperature power spectra were computed using the Cosmic Linear Anisotropy Solving System Boltzman code (CLASS; Blas, Lesgourgues & Tram 2011; Lesgourgues & Tram 2014) and MCMC chains were generated with the MontePython sampler (Audren et al. 2013).

Fig. 7 presents the two-dimensional marginalized 95 per cent credible regions for these two models, and the bottom of Table 4 reports the 1D marginalized posterior median values and 1σ uncertainties of the corresponding model parameters. We note that this time, the TDSL and Planck 95 per cent credible regions are in much better agreement than in the one-parameter extension models. In the $N_{\rm eff}m_\nu\Lambda$CDM cosmology, Planck alone and Planck+CMBL are in agreement with the standard cosmological prediction of $N_{\rm eff}$, yet the constraints are rather large. When adding TDSL, the constraints are strongly tightened and we obtain $N_{\rm eff} = 3.44 \pm 0.24$, in mild tension with the standard cosmological prediction of $N_{\rm eff} = 3.046$. Similarly, the constraints on the maximum neutrino mass are tightened by a factor $\simeq 3$ when adding TDSL, yielding $\Sigma m_\nu \leq 0.274$ eV with 95 per cent probability. In the owCDM cosmology, Planck+CMBL+TDSL yields $\Omega_{\rm k} = -0.003^{+0.004}_{-0.004}$, in good agreement with Planck+CMBL+BAO and in favour of a flat universe. However, a tension in the dark energy equation of state w still remains, as Planck+CMBL+TDSL yields $w = -1.37^{-0.23}_{+0.18}$, 2σ lower than the cosmological constant prediction.

6 CONCLUSIONS

Using multiple telescopes in the Southern and Northern hemispheres, we have monitored the quadruple-imaged strong gravitational lens HE 0435−1223 for 13 yr with an average cadence of one observing epoch every 3.6 d. We analyse the imaging data

using the MCS deconvolution algorithm (Magain et al. 1998) on a total of 876 observing epochs to produce the light curves of the four lensed images, with an rms photometric precision of 10 mmag on the brightest quasar image.

We measured the time delays between each pair of lensed images using the free-knot spline technique and the regression difference technique from the PYCS package (Tewes et al. 2013a). Our uncertainty estimation involves the generation of synthetic light curves that closely mimic the intrinsic and extrinsic features of the real data. To test the robustness of our measurements, we vary parameters such as the number of knots in the splines, the initial parameters used for the deconvolution photometry and the length of the considered light curves. The two curve shifting techniques agree well with each other both on the point estimation of the delays and on the estimated uncertainty. The smallest relative uncertainty, of 6.5 per cent, is obtained for the A-D pair of images. For this pair involving image A, our present measurement is twice as precise as the earlier result by Courbin et al. (2011).

In H0LiCOW Paper IV, we use our new COSMOGRAIL time delays for HE 0435−1223 to compute its time-delay distance. Very importantly, this is done in a blind way with respect to the inference of cosmological parameters. In this paper, we combine the time-delay distance likelihoods from HE 0435−1223 with the published ones from B1608+656 and RXJ1131−1231 to create a TDSL probe. We also combine the latter with other cosmological probes such as *WMAP*, Planck, BAO and JLA to constrain cosmological parameters for a large range of extended cosmological models. Our main conclusions are as follows.

(i) TDSL alone is weakly sensitive to the matter density, $\Omega_{\rm m}$, curvature, $\Omega_{\rm k}$ and dark energy density $\Omega_{\rm de}$ and equation of state w. Its primary sensitivity to H_0 allows us to break degeneracies of CMB probes in extended cosmological models.

(ii) In a flat-ΛCDM cosmology with uniform priors on H_0 and $\Omega_{\rm m}$, TDSL alone yields $H_0 = 71.9^{+2.4}_{-3.0}$ km s^{-1} Mpc^{-1}. When enforcing $\Omega_{\rm m}$=0.32 from the most recent Planck results, we find $H_0 = 72.8 \pm 2.4$ km s^{-1} Mpc^{-1}. These results are in excellent agreement with the most recent measurements using the distance ladder, but are in tension with the CMB measurements from Planck.

(iii) In a non-flat-ΛCDM cosmology, we find, using TDSL and Planck, $H_0 = 69.2^{+1.4}_{-2.2}$ km s^{-1} Mpc^{-1} and $\Omega_{\rm k} = 0.003^{+0.004}_{-0.006}$ in agreement with a flat universe.

(iv) In a flat-wCDM cosmology in combination with Planck, we find a 2.3σ tension from a cosmological constant in favour of a phantom form of dark energy. Our joint constraints in this cosmology are $H_0 = 79.0^{+4.4}_{-4.2}$ km s^{-1} Mpc^{-1}, $\Omega_{\rm de} = 0.77^{+0.02}_{-0.03}$ and $w = -1.38^{+0.14}_{-0.16}$.

(v) In a flat-$m_\nu\Lambda$CDM cosmology, in combination with Planck and BAO we tighten the constraints on the maximum mass of neutrinos to $\Sigma m_\nu \leq 0.182$ eV, while removing the tension in H_0.

(vi) In a flat-$N_{\rm eff}\Lambda$CDM cosmology, in combination with Planck and BAO we find $N_{\rm eff} = 3.34 \pm 0.21$, i.e. 1.3σ higher than the standard cosmological value. This mild tension remains when the constraints on both Σm_ν and $N_{\rm eff}$ are relaxed.

(vii) In a owCDM cosmology, in combination with Planck and CMBL, we find $H_0 = 77.9^{+5.0}_{-4.2}$ km s^{-1} Mpc^{-1}, $\Omega_{\rm de} = 0.77^{+0.03}_{-0.03}$, $\Omega_{\rm k} = -0.003^{+0.004}_{-0.004}$ and $w = -1.37^{+0.18}_{-0.23}$. Similarly to the o$\Lambda$CDM and wCDM cosmologies, we are in good agreement with a flat universe and in tension with a cosmological constant, respectively.

We emphasize that despite reporting parameter constraints for a large variety of cosmological models beyond ΛCDM, we choose not to comment on whether a particular model is favoured over the others. Such an exercise would require a well-motivated choice of priors for these models, which is not within the scope of this work.

The combined strengths of our H0LiCOW lens modelling and COSMOGRAIL monitoring indicate that quasar time-delay cosmography is now a mature field, producing precise and accurate inferences of cosmological parameters, that are independent of any other cosmological probe. Still, our results can be improved in at least four ways.

(i) Continuing to enlarge the sample. Two more objects with excellent time-delay measurements as well as high-resolution imaging and spectroscopic data remain to be analysed in the H0LiCOW project (see H0LiCOW Paper I). When completed, H0LiCOW is expected to provide a measurement of H_0 to better than 3.5 per cent in a non-flat-ΛCDM universe with flat priors on $\Omega_{\rm m}$ and Ω_{Λ}. Data of quality comparable to those obtained for H0LiCOW are in the process of being obtained for another four systems with measured time delays from COSMOGRAIL (HST-GO-14254; PI: Treu). Meanwhile, current and planned wide field imaging surveys such as DES, KiDS, HSC, LSST, *Euclid* and WFIRST, should discover hundreds of new gravitational lens systems suitable for time-delay cosmography (Oguri & Marshall 2010). For example, the dedicated search in the Dark Energy Survey STRIDES[9] has already confirmed two new lenses from the Year1 data (Agnello et al. 2016).

(ii) Improve the lens modelling accuracy. The tests carried out in our current (H0LiCOW Paper IV) and past work (Suyu et al. 2014), the good internal agreement between the three measured systems (Section 5.1), and independent analysis based on completely independent codes (Birrer et al. 2016), show that our lens models are sufficiently complex given the currently available data. However, as the number of systems being analysed grows, random uncertainties in the cosmological parameters will fall, and residual systematic uncertainties related to degeneracies inherent to gravitational lensing will need to be investigated in more detail. Following the work of Xu et al. (2016), detailed hydro *N*-body simulations of lensing galaxies in combination with ray-shooting can be used to evaluate the impact of the lensing degeneracies on cosmological results in view of future observations with the JWST or 30-m class ground-based telescopes with adaptive optics, and to drive development of improved lens modelling techniques and assumptions appropriate to the density structures we expect.

(iii) Improve the absolute mass calibration. Spatially resolved 2D kinematics of the lens galaxies, to be obtained either with JWST and with integral field spectrographs mounted on large ground-based telescopes with adaptive optics, should further improve both the precision for each system and our ability to test for residual systematics, including those arising from the mass sheet and SPT (Schneider & Sluse 2013, 2014; Unruh et al. 2016). The same data should also allow us to use constraints from the stellar mass or mass profile of lens galaxies as attempted in Courbin et al. (2011) with slit spectroscopy. Alternatively, the MSD can be lifted if the absolute luminosity of the source is known (Falco et al. 1985), which is the case for lensed standard candles (see e.g. Goobar et al. 2016, that report the first discovery of a lensed Type Ia Supernovae). However, such configurations happens far less often than lensed quasars.

(iv) Measuring time delays with the current photometric precision and time sampling of monitoring data requires long and time-consuming campaigns, and is currently not possible for hundreds of objects. Increasing the monitoring efficiency is possible, by

---

[9] strides.astro.ucla.edu

catching extremely small (mmag) and fast (days) variations in the quasar light curves. Such data can be obtained with daily observations with 2-m class telescopes in good seeing conditions, a project that will be implemented in the context of the extended COSMOGRAIL programme (eCOSMOGRAIL; Courbin et al. 2016, in preparation) to measure quasar time delays in only one or two observing seasons. Furthermore, in the long run, LSST should be able to provide sufficiently accurate time delays for hundreds of systems from the survey data itself (Liao et al. 2015), and enable subpercent precision on H_0 in the next decade (Treu & Marshall 2016).

REFERENCES

Addison G. E., Huang Y., Watts D. J., Bennett C. L., Halpern M., Hinshaw G., Weiland J. L., 2016, ApJ, 818, 132
Agnello A., Sonnenfeld A., Suyu S. H., Treu T., Fassnacht C. D., Mason C., Bradač M., Auger M. W., 2016, MNRAS, 458, 3830
Anderson L. et al., 2012, MNRAS, 427, 3435
Audren B., Lesgourgues J., Benabed K., Prunet S., 2013, J. Cosmol. Astropart. Phys., 2, 001
Bennett C. L. et al., 2013, ApJS, 208, 20
Bertin E., Arnouts S., 1996, A&AS, 117, 393
Betoule M. et al., 2013, A&A, 552, A124
Beutler F. et al., 2011, MNRAS, 416, 3017
Birrer S., Amara A., Refregier A., 2016, J. Cosmol. Astropart. Phys., 08, 020
Blackburne J. A., Kochanek C. S., Chen B., Dai X., Chartas G., 2014, ApJ, 789, 125
Blake C. et al., 2011, MNRAS, 418, 1707
Blas D., Lesgourgues J., Tram T., 2011, Astrophysics Source Code Library, record ascl:1106.020
Bonamente M., Joy M. K., LaRoque S. J., Carlstrom J. E., Reese E. D., Dawson K. S., 2006, ApJ, 647, 25
Bonvin V., Tewes M., Courbin F., Kuntzer T., Sluse D., Meylan G., 2016, A&A, 585, A88
Braibant L., Hutsemékers D., Sluse D., Anguita T., García-Vergara C. J., 2014, A&A, 565, L11
Cantale N., Courbin F., Tewes M., Jablonka. P., Meylan G., 2016, A&A, 589, A81
Chen G. C. F. et al., 2016, MNRAS, 462, 3457
Collett T. E., Auger M. W., 2014, MNRAS, 443, 969
Collett T. E. et al., 2013, MNRAS, 432, 679
Courbin F., Eigenbrod A., Vuissoz C., Meylan G., Magain P., 2005, in Mellier Y., Meylan G., eds, Proc. IAU Symp. 225, Gravitational Lensing Impact on Cosmology. Cambridge Univ. Press, Cambridge, p. 297
Courbin F. et al., 2011, A&A, 536, A53
Di Valentino E., Melchiorri A., Silk J., 2016, Phys. Lett. B, 761, 242
Dobler G., Fassnacht C. D., Treu T., Marshall P., Liao K., Hojjati A., Linder E., Rumbaugh N., 2015, ApJ, 799, 168
Efstathiou G., 2014, MNRAS, 440, 1138
Eigenbrod A., Courbin F., Dye S., Meylan G., Sluse D., Vuissoz C., Magain P., 2006a, A&A, 451, 747
Eigenbrod A., Courbin F., Meylan G., Vuissoz C., Magain P., 2006b, A&A, 451, 759
Eulaers E. et al., 2013, A&A, 553, A121
Falco E. E., Gorenstein M. V., Shapiro I. I., 1985, ApJ, 289, L1
Fassnacht C. D., Xanthopoulos E., Koopmans L. V. E., Rusin D., 2002, ApJ, 581, 823
Fassnacht C. D., Gal R. R., Lubin L. M., McKean J. P., Squires G. K., Readhead A. C. S., 2006, ApJ, 642, 30
Fassnacht C. D., Koopmans L. V. E., Wong K. C., 2011, MNRAS, 410, 2167
Freedman W. L., Madore B. F., Scowcroft V., Burns C., Monson A., Persson S. E., Seibert M., Rigby J., 2012, ApJ, 758, 24
Gao F. et al., 2016, ApJ, 817, 128
Giusarma E., Gerbino M., Mena O., Vagnozzi S., Ho S., Freese K., 2016, Phys. Rev. D, 94, 083522
Goobar A. et al., 2016, preprint (arXiv:1611.00014)
Greene Z. S. et al., 2013, ApJ, 768, 39
Heavens A., Jimenez R., Verde L., 2014, Phys. Rev. Lett., 113, 241302
Heymans C. et al., 2012, MNRAS, 427, 146
Hilbert S., White S. D. M., Hartlap J., Schneider P., 2007, MNRAS, 382, 121
Hilbert S., Hartlap J., White S. D. M., Schneider P., 2009, A&A, 499, 31
Hinshaw G. et al., 2013, ApJS, 208, 19
Kochanek C. S., 2002, ApJ, 578, 25

Kochanek C. S., Morgan N. D., Falco E. E., McLeod B. A., Winn J. N., Dembicky J., Ketzeback B., 2006, ApJ, 640, 47

Lesgourgues J., Tram T., 2014, J. Cosmol. Astropart. Phys., 9, 032

Lewis A., Bridle S., 2002, Phys. Rev. D, 66, 103511

Liao K. et al., 2015, ApJ, 800, 11

Linder E. V., 2011, Phys. Rev. D, 84, 123529

McCully C., Keeton C. R., Wong K. C., Zabludoff A. I., 2014, MNRAS, 443, 3631

McCully C., Keeton C. R., Wong K. C., Zabludoff A. I., 2016, preprint (arXiv:1601.05417)

Magain P., Courbin F., Sohy S., 1998, ApJ, 494, 472

Marshall P., Rajguru N., Slosar A., 2006, Phys. Rev. D, 73, 067302

Molinari N., Durand J., Sabatier R., 2004, Comput. Stat. Data Anal., 45, 159

Momcheva I. G., Williams K. A., Cool R. J., Keeton C. R., Zabludoff A. I., 2015, ApJS, 219, 29

Morgan N. D., Kochanek C. S., Pevunova O., Schechter P. L., 2005, AJ, 129, 2531

Oguri M., Marshall P. J., 2010, MNRAS, 405, 2579

Padmanabhan N., Xu X., Eisenstein D. J., Scalzo R., Cuesta A. J., Mehta K. T., Kazin E., 2012, MNRAS, 427, 2132

Pelt J., Kayser R., Refsdal S., Schramm T., 1996, A&A, 305, 97

Percival W. J. et al., 2010, MNRAS, 401, 2148

Planck Collaboration XVI, 2014, A&A, 571, A16

Planck Collaboration XIII, 2016a, A&A, 594, A13

Planck Collaboration XV, 2016b, A&A, 594, A15

Planck Collaboration XVIII, 2016c, A&A, 594, A18

Rathna Kumar S. et al., 2013, A&A, 557, A44

Refsdal S., 1964, MNRAS, 128, 307

Riess A. G. et al., 2016, ApJ, 826, 56

Rigault M. et al., 2015, ApJ, 802, 20

Salvatelli V., Marchini A., Lopez-Honorez L., Mena O., 2013, Phys. Rev. D, 88, 023531

Schneider P., Sluse D., 2013, A&A, 559, A37

Schneider P., Sluse D., 2014, A&A, 564, A103

Sluse D., Tewes M., 2014, A&A, 571, A60

Sluse D., Hutsemékers D., Courbin F., Meylan G., Wambsganss J., 2012, A&A, 544, A62

Sorce J. G., Tully R. B., Courtois H. M., 2012, ApJ, 758, L12

Spergel D. N., Flauger R., Hložek R., 2015, Phys. Rev. D, 91, 023518

Suyu S. H., Halkola A., 2010, A&A, 524, A94

Suyu S. H., Marshall P. J., Hobson M. P., Blandford R. D., 2006, MNRAS, 371, 983

Suyu S. H., Marshall P. J., Auger M. W., Hilbert S., Blandford R. D., Koopmans L. V. E., Fassnacht C. D., Treu T., 2010, ApJ, 711, 201

Suyu S. H. et al., 2012, ApJ, 750, 10

Suyu S. H. et al., 2013, ApJ, 766, 70

Suyu S. H. et al., 2014, ApJ, 788, L35

Tewes M., Courbin F., Meylan G., 2013a, A&A, 553, A120

Tewes M. et al., 2013b, A&A, 556, A22

Treu T., 2010, ARA&A, 48, 87

Treu T., Marshall P. J., 2016, A&AR, in press

Unruh S., Schneider P., Sluse D., 2016, preprint (arXiv:1606.04321)

Weinberg D. H., Mortonson M. J., Eisenstein D. J., Hirata C., Riess A. G., Rozo E., 2013, Phys. Rep., 530, 87

Wisotzki L., Christlieb N., Bade N., Beckmann V., Köhler T., Vanelle C., Reimers D., 2000, A&A, 358, 77

Wisotzki L., Schechter P. L., Bradt H. V., Heinmüller J., Reimers D., 2002, A&A, 395, 17

Wong K. C., Keeton C. R., Williams K. A., Momcheva I. G., Zabludoff A. I., 2011, ApJ, 726, 84

Wucknitz O., 2002, MNRAS, 332, 951

Xu D., Sluse D., Schneider P., Springel V., Vogelsberger M., Nelson D., Hernquist L., 2016, MNRAS, 456, 739

[1]*Laboratory of Astrophysics, Institute of Physics, Ecole Polytechnique Fédérale de Lausanne (EPFL), Observatoire de Sauverny, CH-1290 Versoix, Switzerland*

[2]*Max Planck Institute for Astrophysics, Karl-Schwarzschild-Strasse 1, D-85740 Garching, Germany*

[3]*Physik-Department, Technische Universität München, James-Franck-Straße 1, D-85748 Garching, Germany*

[4]*Institute of Astronomy and Astrophysics, Academia Sinica, PO Box 23-141, Taipei 10617, Taiwan*

[5]*Kavli Institute for Particle Astrophysics and Cosmology, Stanford University, 452 Lomita Mall, Stanford, CA 94035, USA*

[6] *Department of Physics, University of California, Davis, CA 95616, USA*

[7]*STAR Institute, Quartier Agora - Allée du six Août, 19c B-4000 Liège, Belgium*

[8]*Argelander-Institut für Astronomie, Auf dem Hügel 71, D-53121 Bonn, Germany*

[9]*National Astronomical Observatory of Japan, 2-21-1 Osawa, Mitaka, Tokyo 181-8588, Japan*

[10]*Institute of Cosmology and Gravitation, University of Portsmouth, Burnaby Rd, Portsmouth PO1 3FX, UK*

[11]*Department of Physics and Astronomy, University of California, Los Angeles, CA 90095, USA*

[12]*Institute of Astronomy, University of Cambridge, Madingley Road, Cambridge CB3 0HA, UK*

[13]*Exzellenzcluster Universe, Boltzmannstr. 2, D-85748 Garching, Germany*

[14]*Ludwig-Maximilians-Universität, Universitäts-Sternwarte, Scheinerstr. 1, D-81679 München, Germany*

[15]*Kapteyn Astronomical Institute, University of Groningen, PO Box 800, NL-9700-AV Groningen, The Netherlands*

[16]*Kavli IPMU (WPI), UTIAS, The University of Tokyo, Kashiwa, Chiba 277-8583, Japan*

[17]*Physics Department, University of California, Santa Barbara, CA 93106, USA*

This paper has been typeset from a TₑX/LᴬTₑX file prepared by the author.